# A first-order statistical exploration of the mathematical limits of Micromagnetic Tomography

Frenk Out[1,1,1], David Cortés-Ortuño[1,1,1], Karl Fabian[2,2,2], Tristan van Leeuwen[1,1,1], and Lennart de Groot[1,1,1]

[1]Utrecht University
[2]Norwegian University of Science and Technology (NTNU)

November 30, 2022

**Abstract**

The recently developed Micromagnetic Tomography (MMT) technique combines advances in high resolution scanning magnetometry and micro X-ray computed tomography. This allows precise recovery of magnetic moments of individual magnetic grains in a sample using a least-squares inversion approach. Here we investigate five factors, which are governing the mathematical validity of MMT solutions: grain concentration, thickness of the sample, size of the sample's surface, noise level in the magnetic scan, and sampling interval of the magnetic scan. To compute the influence of these parameters, we set up series of numerical models in which we assign dipole magnetizations to randomly placed grains. Then we assess how well their magnetizations are resolved as function of these parameters. We expanded the MMT inversion to also produce the covariance and standard deviations of the solutions, and use these to define a statistical uncertainty ratio and signal strength ratio for each solution. We show that the magnetic moments of a majority of grains under the inspected conditions are solved with very small uncertainties. However, increasing the grain density and sample thickness carry major challenges for the MMT inversions, demonstrated by uncertainties larger than 100% for some grains. Fortunately, we can use the signal strength ratio to extract grains with the most accurate solutions, even from these challenging models. Hereby we have developed a quick and objective routine to individually select the most reliable grains from MMT results. This will ultimately enable determining paleodirections and paleointensities from large subsets of grains in a sample using MMT.

# A first-order statistical exploration of the mathematical limits of Micromagnetic Tomography

**Frenk Out[1], David Cortés-Ortũno[1], Karl Fabian[2], Tristan van Leeuwen[3,4], Lennart V. de Groot[1]**

[1]Paleomagnetic laboratory Fort Hoofddijk, Department of Earth Sciences, Utrecht University, Budapestlaan 17, 3584 CD Utrecht, The Netherlands.
[2]Norwegian University of Science and Technology (NTNU), S. P. Andersens veg 15a, 7031 Trondheim, Norway
[3]Mathematical Institute, Faculty of Sciences, Utrecht University, Utrecht, The Netherlands
[4]Department of Computational Imaging, Centrum Wiskunde & Informatica (CWI), The Netherlands

**Key Points:**

- The mathematical performance of Micromagnetic Tomography is tested against the sample's geometry, instrumental noise and sampling interval
- Sample thickness and grain density are the prime factors controlling the theoretical uncertainty of magnetic moments of individual grains
- The mathematical accuracy of Micromagnetic Tomography results can be assessed using the signal strength ratio and uncertainty ratio

Corresponding author: Frenk Out, `f.out@uu.nl`

## Abstract

The recently developed Micromagnetic Tomography (MMT) technique combines advances in high resolution scanning magnetometry and micro X-ray computed tomography. This allows precise recovery of magnetic moments of individual magnetic grains in a sample using a least-squares inversion approach. Here we investigate five factors, which are governing the mathematical validity of MMT solutions: grain concentration, thickness of the sample, size of the sample's surface, noise level in the magnetic scan, and sampling interval of the magnetic scan. To compute the influence of these parameters, we set up series of numerical models in which we assign dipole magnetizations to randomly placed grains. Then we assess how well their magnetizations are resolved as function of these parameters. We expanded the MMT inversion to also produce the covariance and standard deviations of the solutions, and use these to define a statistical uncertainty ratio and signal strength ratio for each solution. We show that the magnetic moments of a majority of grains under the inspected conditions are solved with very small uncertainties. However, increasing the grain density and sample thickness carry major challenges for the MMT inversions, demonstrated by uncertainties larger than 100% for some grains. Fortunately, we can use the signal strength ratio to extract grains with the most accurate solutions, even from these challenging models. Hereby we have developed a quick and objective routine to individually select the most reliable grains from MMT results. This will ultimately enable determining paleodirections and paleointensities from large subsets of grains in a sample using MMT.



## Plain Language Summary

Iron-bearing rocks have the ability to capture and store the direction and strength of Earth's magnetic field. This information is used to unravel the behavior of the magnetic field that protects us from harmful solar radiation. However, obtaining a reliable signal from these rocks is difficult using existing methods because many iron-oxide grains exhibit complex magnetic behavior and obscure the magnetic information in them. To determine magnetic moments from individual grains, a new method known as Micromagnetic Tomography has been developed. This method works similarly to imaging techniques in hospitals, but now a thin slice of rock containing magnetic grains is scanned. By using computer models we discovered that Micromagnetic Tomography is able to reliably extract magnetic signals from a majority of grains in many rock samples. Addi-

tionally, we have developed two new parameters that help us to easily select the magnetic moments of the most reliable grains in a sample. In this way the signal of those grains can be effectively used to provide accurate information on the present and past state of Earth's magnetic field.

## 1 Introduction

Obtaining a reliable characteristic remanent magnetization (ChRM) from volcanic rock samples is an important challenge in paleomagnetism. Volcanic rocks acquire a thermoremanent magnetization (TRM) when they cool in the Earth's magnetic field that is proporational to the direction and strength of the magnetic field at the time of cooling. TRMs of natural rocks are often regarded to be the most reliable data source for geomagnetic field models because of their ability to store information on the paleomagnetic field for thousands to millions of years (e.g. Panovska et al., 2019; Pavón-Carrasco et al., 2021). Full vector ChRMs consist of both directional and intensity information on the past geomagnetic field, but they can generally only be obtained for 10% to 20% of volcanic samples carrying TRMs (e.g. Tauxe & Yamazaki, 2015; Nagy et al., 2017). One of the reasons for the low success rates is that only single domain (SD) or pseudo-single domain (PSD) iron oxide grains, typically with diameters $< 1$ $\mu$m, are reliable recorders of the Earth's magnetic field. Larger multidomain (MD) grains are typically prone to more unstable magnetic moments (Néel, 1955; Fabian, 2000, 2001). Natural rocks commonly contain a wide range of iron-oxide particle sizes. Magnetically adverse behaved MD grains are therefore often present. When measuring bulk rock samples the measured magnetic moment is a statistical summation of all the magnetic grains in the sample. The presence of MD grains therefore often explains the low success rate of extracting a reliable full vector bulk ChRM.

A solution to this problem would be to differentiate between signals stored in small and large grains by determining the magnetic moment of each iron-oxide grain in a sample separately. To obtain all individual magnetic moments, the magnetic flux above a thin sample produced by all grains inside is measured on a micrometer scale. Such a map of the magnetic flux with the necessary resolution in space and magnetic moments can be obtained from a scanning superconducting quantum interference device (SQUID; e.g. Egli & Heller, 2000; Weiss et al., 2007; de Groot et al., 2018) or a quantum diamond magnetometer (QDM; e.g. Glenn et al., 2017; Farchi et al., 2017; de Groot et al., 2021). Unfortunately, this is not sufficient to reconstruct the magnetic moments of individual grains inside the sample. To reduce the number of unknown variables in the inversion, the position of the magnetic grains must be constrained further. Weiss et al. (2007), for example, applied a constraint related to the dipolar magnetization of all grains, by assuming that the magnetization for all grains is uniform in intensity and direction. The magnetic signal of grains close to the sensors that detect the surface magnetic field, however, is better modeled using multipoles than dipoles (Cortés-Ortuño et al., 2021). Additionally, since shapes and volumes of grains can vary, it appears unlikely that the magnetization of all grains are uniform in intensity and direction (Dunlop & Özdemir, 1997). To avoid further assumptions on the positions of grains, de Groot et al. (2018) employed micro X-Ray Computed Tomography (MicroCT) to exactly determine these positions. By combining MicroCT with the surface magnetic field obtained by magnetometry the resulting mathematical inversion problem becomes well posed (Fabian & De Groot, 2019), and it is possible to compute the individual magnetic moments of every grain in the sample. It was recently shown that not only the dipole component of the grain's magnetic moments can be recovered, but also higher order multipole components can be determined (Cortés-Ortuño et al., 2021). This technique of combining scanning magnetometry data with MicroCT analyses to constrain the mathematical inversion and obtain magnetic moments of individual grains in a sample is now known as Micromagnetic Tomography (MMT).

Although the potential of MMT was illustrated by de Groot et al. (2018, 2021), significant challenges remain before this new technique is of experimental value for paleomagnetic and rock-magnetic studies. These challenges are of empirical nature on one hand, and of both mathematical and computational nature on the other. Examples of empirical challenges are the resolution of the MicroCT and magnetic scanning techniques, mapping between the two data-sets and applying routine paleomagnetic and rock-magnetic treatments to the samples in the MMT workflow. Here, however, we focus on computational and mathematical challenges that remain, and provide a theoretical framework on how to obtain and treat uncertainties arising from MMT inversions. Furthermore, we provide new statistical parameters that describe and scrutinize MMT results and are therefore necessary to address the standing empirical challenges.

To assess the accuracy and uncertainty associated with magnetic moments of individual grains obtained with MMT, we consider five different factors that may substantially affect the theoretical uncertainty of MMT solutions: (1) the thickness of the sample, (2) the area covered by the surface magnetic scan, (3) the grain density of the rock sample, (4) the distance between adjacent measurement points on the surface, and (5) the instrumental noise level of the surface magnetometry. We design numerical models to cover all combinations of these five factors. To determine the quality of the uniform magnetic moments as determined by MMT in a spherical coordinate frame, we define a 95% confidence interval that we obtain from bootstrapping the covariance matrix produced by the MMT inversion. The 95% confidence interval gives a quantitative indication of the mathematical accuracy of the solution in a single parameter. Additionally, we evolve the $V/R^3$-ratio (Cortés-Ortuño et al., 2021) that relates the depth and volume of a grain to the strength of the magnetic signal that the grain can potentially produce on the surface of the sample, into the 'signal strength ratio'. We then use this signal strength ratio (SSR) to quickly discern which grains are solved with high confidence. Finally, we discuss the implications of our results on obtaining highly accurate ChRM measurements.

We selected five parameters for our study to assess the response of the accuracy of MMT results to variations in these boundary conditions. There are undoubtedly more factors influencing MMT solutions, but they are mostly of empirical nature, e.g. grains not recognized by MicroCT, and co-registration errors related to spatial distortions between MicroCT data and magnetic field data. These factors are challenging to model and depend primarily on the technical details and configurations of the instruments involved. They are therefore better solved by a technical assessment than by mathematical simulations. Furthermore, our study is limited in that we only assign representative uniform (i.e., dipolar) magnetic moments to all grains in our models; although multipole moments may be more realistic for the larger grains included. The MMT studies to date, however, mostly use this dipole approximation in their inversions; MMT studies using higher order, multipole, moments were proposed only recently (Cortés-Ortuño et al., 2021). The statistical parameters to assess and scrutinize MMT results that we propose here will be applicable to higher order MMT results as well.

# 2 Methods

## 2.1 Model design

The inversion routine we use here closely follows the procedure as described in de Groot et al. (2018, 2021), but we first define synthetic models given the five parameters that we consider in this study. This requires populating 'sample volumes' with grains in random locations and assigning them a somewhat realistic uniform magnetization. Then we calculate the map of the magnetic flux on the surface of the sample and perturb these maps with realistic noise. Once the sample volumes and magnetic flux map are deter-

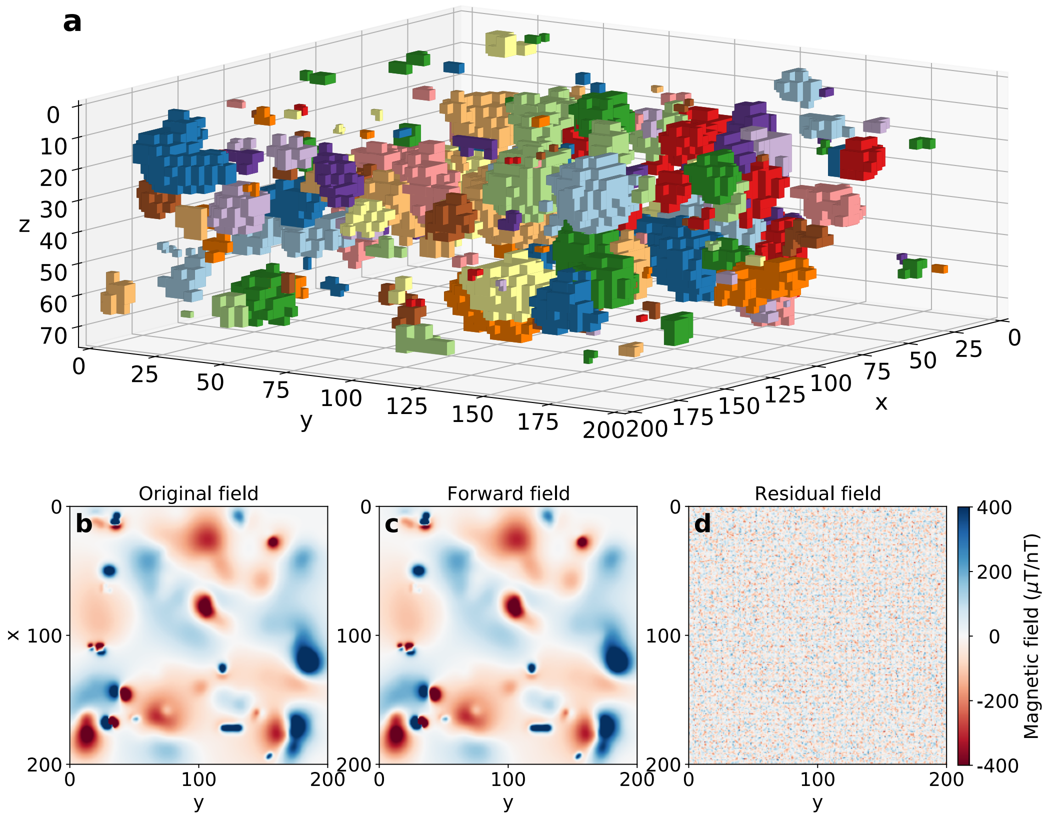


**Figure 1.** The MMT workflow of one of our models containing 75,000 grains per mm$^3$ with a dipolar magnetization. a) Geometric overview of the model with a $200\times200$ $\mu$m$^2$ sample surface size. Each grain is assigned a color for clarity, the colors do not have further meaning. The sensor grid is located on top of the model at $z = 0$. Each grain is build from rectangular shaped cuboids. b) Original magnetic field created by the signal of the grains and after adding noise with a level of 100 nT. c) Magnetic field produced by the signal of grains with the inverted magnetization values. The unit of field strength in b) and c) is $\mu$T. d) Residual field obtained by subtracting the original field in b) from the forward field based on the inversion result in c). The unit of field strength in d) is nT.

**Table 1.** Parameters changed between models. Every possible combination of parameters is assessed in this study, resulting in 448 models. Each model is then ran 15 times to ensure statistically robust results.

| Parameter | Unit | Modeled values |
|---|---|---|
| Sample surface size | $\mu$m$^2$ | 200×200, 500×500 |
| Sample thickness | $\mu$m | 50, 75 |
| Grain density | $10^3$ grains per mm$^3$ | 2.5, 5.0, 10.0, 25.0 |
| | | 50.0, 75.0, 100.0 |
| Sampling interval | $\mu$m | 1, 2, 4, 5 |
| Noise level | nT | 5, 20, 50, 100 |

mined we apply the inversion routine but also produce the standard deviations associated with the individual magnetic moments. Lastly, we define the 95% confidence interval of magnetic moments to assess the performance of MMT as a function of the five input parameters for the models.

#### *2.1.1 Populating sample volumes*

To define the input of the inversions we start with a rectangular sample volume with a predefined, rectangular, surface size and a set sample thickness. Inside this volume a number of modeled iron-oxide grains are randomly placed such that they do not intersect. The number and average volume of these grains determine the modeled iron-oxide grain density. We modeled samples with an area of 200 × 200 and 500 × 500 $\mu$m$^2$. The maximum thickness of the models was either 50 or 75 $\mu$m (Table 1). The individual grains used to populate the models with were taken from the actual geometries obtained from a MicroCT scan of a volcanic sample prepared from a sister sample of HW03 (de Groot et al., 2013; ter Maat et al., 2018; de Groot et al., 2021). This sample was obtained from a lava flow active in 1907 on Hawaii. The sample was drilled at an elevation of 603 m (±4 m) with a latitude of 19° 4.315' and a longitude of 155° 44.314'. The sample was reduced to a thickness of 80 $\mu$m, after which the location and size of its magnetic grains were obtained with MicroCT. The MicroCT outputted each grain as a list of voxels with an elementary volume of 0.75 × 0.75 × 0.75 $\mu$m$^3$. The individual voxels were combined into a minimum amount of rectangular shaped cuboids, which together composed one grain, for optimization purposes. The MicroCT data showed that all grains have a diameter between 1 and 20 $\mu$m. We populated the models with these grains without changing their orientation until the respective grain density was reached, which is specified in Table 1. By using this range of grain densities, the models simulated both the low grain density of the synthetic sample of de Groot et al. (2018) and the high grain density of the volcanic sample of de Groot et al. (2021). Each grain was then placed at a random location within the model such that it does not intersect another grain or the boundaries of the model (Fig. 1a). This random placement routine has been made more efficient by imposing that the top side of each grain could only be placed between the surface of the sample and 10 $\mu$m from the bottom of the sample, since most grains have diameters smaller than 10 $\mu$m. The sample thickness for some models could, therefore, be less than the indicated value. If the grain did not fit at the given location, we retried placing the grain up to a hundred times. If the grain did not fit by then, we selected at random another grain geometry and tried to fit the new grain up to a hundred times again.

#### *2.1.2 Assigning realistic magnetizations*

In the next step, each individual grain was assigned a random magnetization $\mathbf{M}$ = ($M_x$, $M_y$, $M_z$), where $|\mathbf{M}|$ denotes its magnitude. Therefore, we treat all grains as equivalent single domain grains. This implies that the cuboid components of each grain have the same strength and direction of magnetization as the whole grain. To obtain realistic magnetization values, the value of $|\mathbf{M}|$ was chosen to agree with the magnetization versus grain diameter trend for a natural volcanic sample presented in Fig. 4D of de Groot et al. (2021). This trend is a SD grain magnetization representation of the magnetization intensity of PSD and MD grains and is in good agreement to the relation between the relative magnetization as function of grain diameter in Fig. 29 of Dunlop (1990). The trend line in Fig. 4D (de Groot et al., 2021) can be converted to the empirical relation:

$$|\mathbf{M}| = M_0 \ (V/V_0)^{\alpha} \,, \tag{1}$$

where $V_0$ is the volume, and $M_0$ the magnetization of a sphere with diameter 1 $\mu$m; $\alpha$ is the relation parameter, and $|\mathbf{M}|$ is the absolute expected magnetization of a grain with volume $V$. For the trend line in Fig. 4D in de Groot et al. (2021) we obtained: $M_0 =$

46.5 kA/m, and $\alpha = -0.355$. To simulate the spread in the data points that define this relation, we add a perturbation to the magnetizations. To this end the magnetization norm $|\mathbf{M}|$ was multiplied by $10^{N(\mu,\sigma^2)}$, where $N(\mu, \sigma^2)$ represents the Gaussian distribution with a mean, $\mu$, of zero and a variation, $\sigma^2$, of $0.5^2$, to produce the final magnetization norm $|\mathbf{M}_f|$. Hereafter, we sampled the uniform distribution $U(0, 2\pi)$ to obtain the angle $\phi$ of the magnetization vector in the $x-y$-plane. The angle $\theta$ with respect to the $z$-axis was sampled from the uniform distribution $U(0, \pi)$. The norm and the two angles of the magnetization vector were then transformed into the Cartesian components $M_x$, $M_y$, and $M_z$.

#### *2.1.3 Calculating the magnetic flux map*

Once the particle positions and magnetizations are assigned, the grid of measurement points is defined on the surface $z = 0$. The sampling interval of the magnetic flux map is one of the parameters that we investigate in this study, so it is varied to represent different realistic sampling intervals (Table 1). The smallest sampling interval used in the analysis is 1 $\mu$m such that a measurement area of 200 $\times$ 200 $\mu$m$^2$ contains 201 $\times$ 201 (=40,401) measurement points, and a model area of 500 $\times$ 500 $\mu$m$^2$ contains 501 $\times$ 501 (=251,001) measurement points. The largest sampling interval is set to 5 $\mu$m, so that the 200 $\times$ 200 $\mu$m$^2$ surface contains 41 $\times$ 41 (=1,681) data points and the 500 $\times$ 500 $\mu$m$^2$ surface is limited to 101 $\times$ 101 (=10,201) data points.

Now that the grain shapes and locations, and the grid of the measurement points on the surface are determined, the vertical magnetic flux field is calculated in each of the measurement points. The flux field is produced by all uniformly magnetized cuboids belonging to a grain and declines in strength when propagating to the sensors at the surface. To model this behaviour the flux field is represented by a multiplication of the cuboids' magnetization components ($M_x$, $M_y$, and $M_z$) with a corresponding factor $Q$. This factor declines for increasing distance between sensor and cuboid, and is dependent on the direction of the magnetization components. Details for calculating this factor is found in the Supplementary Information of de Groot et al. (2018). All $Q$ factors associated to the cuboids making a single grain are summed per magnetization component. This results in three factors $Q_{xsg}$, $Q_{ysg}$, and $Q_{zsg}$ obtained for a grain $g$ measured at a sensor $s$. To obtain the flux field $\phi_s$ measured at the sensor these factors are multiplied by the magnetization of the grain $M_{xg}$, $M_{yg}$, and $M_{zg}$, respectively, and summed. The total flux field measured at one sensor, however, is not created by one grain but by $K$ grains. For that reason, the total magnetic flux field $\phi_s$ measured at the sensor is a summation over the flux field of $K$ grains, or

$$\begin{aligned}\phi_s &= Q_{xs1}M_{x1} + Q_{ys1}M_{y1} + Q_{zs1}M_{z1} + Q_{xs2}M_{x2} + \ldots + Q_{zsK}M_{zK} \\ &= \begin{bmatrix} Q_{xs1} & Q_{ys1} & Q_{zs1} & Q_{xs2} & \cdots & Q_{zsK} \end{bmatrix} \begin{bmatrix} M_{x1} \\ M_{y1} \\ M_{z1} \\ M_{x2} \\ \vdots \\ M_{zK} \end{bmatrix}.\end{aligned} \tag{2}$$

Since the magnetic flux field is obtained simultaneously at $P$ sensors, the full representation of the forward problem in matrix notation is

$$\begin{bmatrix} \phi_1 \\ \phi_2 \\ \vdots \\ \phi_P \end{bmatrix} = \begin{bmatrix} Q_{x11} & Q_{y11} & Q_{z11} & Q_{x12} & \cdots & Q_{z1K} \\ Q_{x21} & Q_{y21} & Q_{z21} & Q_{x22} & \cdots & Q_{z2K} \\ \vdots & \vdots & \vdots & \vdots & \ddots & \vdots \\ Q_{xP1} & Q_{yP1} & Q_{zP1} & Q_{xP2} & \cdots & Q_{zPK} \end{bmatrix} \begin{bmatrix} M_{x1} \\ M_{y1} \\ M_{z1} \\ M_{x2} \\ \vdots \\ M_{zK} \end{bmatrix}. \tag{3}$$

This forward problem, therefore, consists of $P$ rows and $3 \times K$ columns and will be written in the following short notation,

$$\boldsymbol{\phi} = Q\mathbf{M}_a. \tag{4}$$

In our models the magnetic signal at each measurement point is the total integrated magnetic flux from all grains through a rectangular sensor loop in the $x - y$-plane of the sample with side lengths $1 \times 1$ $\mu$m centered at the measurement point. To simulate the effect of instrumental errors introduced by a magnetometer, $\mathbf{e}$, one of the four noise levels specified in Table 1 was added to the magnetic field of each model, $\tilde{\boldsymbol{\phi}} = \boldsymbol{\phi} + \mathbf{e}$. This adds white noise that is normally distributed with a standard deviation governed by the noise level and with a zero mean to the magnetic surface scan. These noise magnitudes are comparable to those described by Glenn et al. (2017). Now the maps of the magnetic flux at the surface of our models are known (Fig. 1b).

#### *2.1.4 Inversion procedure*

Based on the methods of de Groot et al. (2018), Fabian and De Groot (2019), and de Groot et al. (2021), we used a least-squares minimization to obtain the magnetization of individual grains in the sample, since the inverse problem has a larger number of magnetic flux field observations than unknown magnetization components, *i.e.* $P > 3 \times K$ (Snieder & Trampert, 1999). The magnetization solution, $\widehat{\mathbf{M}}_a$, is given by

$$\widehat{\mathbf{M}}_a = Q^\dagger \tilde{\boldsymbol{\phi}}, \tag{5}$$

with $Q^\dagger$ being the pseudo-inverse of $Q$. The calculated magnetization is used to compute the forward magnetic flux field, $\hat{\boldsymbol{\phi}}$ (Fig. 1c). This forward field is obtained through matrix multiplication of the calculated magnetizations with matrix $Q$, frequently called the Green's matrix,

$$\widehat{\boldsymbol{\phi}} = Q\widehat{\mathbf{M}}_a. \tag{6}$$

Subtracting the initial magnetic field from the forward field results in the residual magnetic field (Fig. 1d).

#### *2.1.5 Varying the input parameters*

For each of the five input parameters we determined a range of realistic values to assess (Table 1). Incorporating all combinations of these five factors yields 448 different computational models, formed by all possible combinations of 2 sample surface areas, 2 sample thicknesses, 7 different grain densities, 4 different sampling intervals, and 4 different noise levels. We executed each of these models fifteen times with different random grain locations and uniform magnetizations to attain enough inversion solutions for a stable and meaningful statistical underpinning of the results. The coarser sampling rates of 2, 4, and 5 $\mu$m grid spacing were simulated by sub-sampling the 1 $\mu$m grid after noise was added. In this way we make sure that each sampling rate uses the same noise contaminated magnetic field.

### 2.2 Uncertainty ratio

#### *2.2.1 Covariance and standard deviation*

The inversion as used for MMT also allows for determining the standard deviation and covariance associated with each solution. To assess the accuracy and uncertainty of the MMT results we define a 95% confidence sphere. The 95% confidence sphere, which is similar to a 95% confidence interval in three dimensions, is obtained per grain through bootstrapping the covariance matrix for each solution that we obtain from the inversion routine. This is done such that if we would repeat the inversion procedure and redraw the Gaussian noise $\mathbf{e}$ a hundred times, we would expect for a grain that 95 out of the 100 associated 95% confidence spheres contain the 'true' correct magnetization, $\mathbf{M}$ (Sim & Reid, 1999). The radius of the confidence sphere gives the precision of the corresponding magnetization solution, where a larger radius indicates a less precise solution.

The 95% confidence sphere is constructed by means of the magnetization solutions $\widehat{\mathbf{M}}_a$ and the covariance matrix $C_{ij}$. The covariance matrix is defined to indicate the expected relationship between two variables $a$ and $b$ relatively to the deviation from their expected values $E[a]$ and $E[b]$. If the covariance between two magnetization variables $M_1$ and $M_2$ is positive, and if $M_2$ is larger than expected, then this implies that $M_1$ will be larger than expected and vice versa. Conversely, if the covariance is negative and if $M_1$ is larger than expected, then this means that $M_2$ will be smaller than the expected value and vice versa. The covariance of a magnetization variable with itself, $C_{ii}$, is always positive and indicates the squared deviation from the expected value, which is frequently called the squared standard deviation. The covariance matrix is mathematically defined as

$$C = E[(\widehat{\mathbf{M}}_a - E[\mathbf{M}_a])(\widehat{\mathbf{M}}_a - E[\mathbf{M}_a])^T]. \tag{7}$$

The value $E[\mathbf{M}_a]$ is known as the expected magnetization, which is the magnetization that would result from perfect magnetic flux observations without any observational noise

$$E[\mathbf{M}_a] = Q^\dagger \boldsymbol{\phi}. \tag{8}$$

Note the similarity between equation (8) and equation (5). If we theoretically obtain a magnetic flux field without any observational noise, then the magnetization calculated through equation (5) is equal to the expected magnetization of equation (8).

By combining equations (5) and (8), we can define $\widehat{\mathbf{M}}_a$ as the sum of perfect observations and instrumental errors $\mathbf{e}$, modeled as Gaussian noise,

$$\begin{aligned}\widehat{\mathbf{M}}_a &= Q^\dagger(\boldsymbol{\phi}+\mathbf{e}) \\ &= Q^\dagger\boldsymbol{\phi} + Q^\dagger\mathbf{e} \\ &= E[\mathbf{M}_a] + Q^\dagger\mathbf{e}, \end{aligned} \tag{9}$$

with $Q^\dagger\mathbf{e}$ being the magnetization error caused by Gaussian instrumental noise. The definition for $\widehat{\mathbf{M}}_a$ in equation (9) is used to simplify equation (7) to

$$\begin{aligned} C &= E[(E[\mathbf{M}_a] + Q^\dagger\mathbf{e} - E[\mathbf{M}_a])(E[\mathbf{M}_a] + Q^\dagger\mathbf{e} - E[\mathbf{M}_a])^T] \\ &= E[(Q^\dagger\mathbf{e})(Q^\dagger\mathbf{e})^T] \\ &= E[Q^\dagger\mathbf{e}\mathbf{e}^T(Q^\dagger)^T]. \end{aligned} \tag{10}$$

The matrix $Q^\dagger$ is the least squares inverse of the Green's matrix $Q$, therefore it is defined as $(Q^TQ)^{-1}Q^T$ (Snieder & Trampert, 1999). The matrix is not a variable, therefore only the expected value of the errors of the magnetic field is left, $E[\mathbf{e}\mathbf{e}^T]$. In this study we assume that the errors of the magnetic field are uncorrelated, because we disregard grain positioning errors caused by MicroCT (de Groot et al., 2018, 2021). Assuming that the errors are uncorrelated, $E[\mathbf{e}\mathbf{e}^T]$ is equal to the squared standard deviation of the error $\mathbf{e}$ times the unit matrix or $\sigma^2 I$. Note that $\sigma$ is the standard deviation of the expected instrumental noise in the data, which is one of the five parameters we vary in this study. Implementing this new expression into equation (10) and rearranging gives the final equation for calculating the covariance matrix

$$\begin{aligned} C &= Q^\dagger E[\mathbf{e}\mathbf{e}^T](Q^\dagger)^T \\ &= Q^\dagger E[\mathbf{e}\mathbf{e}^T]((Q^TQ)^{-1}Q^T)^T \\ &= (\sigma^2(Q^TQ)^{-1})^T = \sigma^2(Q^TQ)^{-1}, \end{aligned} \tag{11}$$

We deduced from equation (7) that the covariance matrix is symmetric. Hence, $(\sigma^2(Q^TQ)^{-1})^T$ is the same as $\sigma^2(Q^TQ)^{-1}$. The inverse of the matrix $Q^TQ$ exists, because the problem is well posed (Fabian & De Groot, 2019). The squared standard deviations of the assigned magnetizations per grain are now found on the main diagonal of the $\sigma^2(Q^TQ)^{-1}$ matrix. The root of the main diagonal therefore gives the standard deviations of the assigned

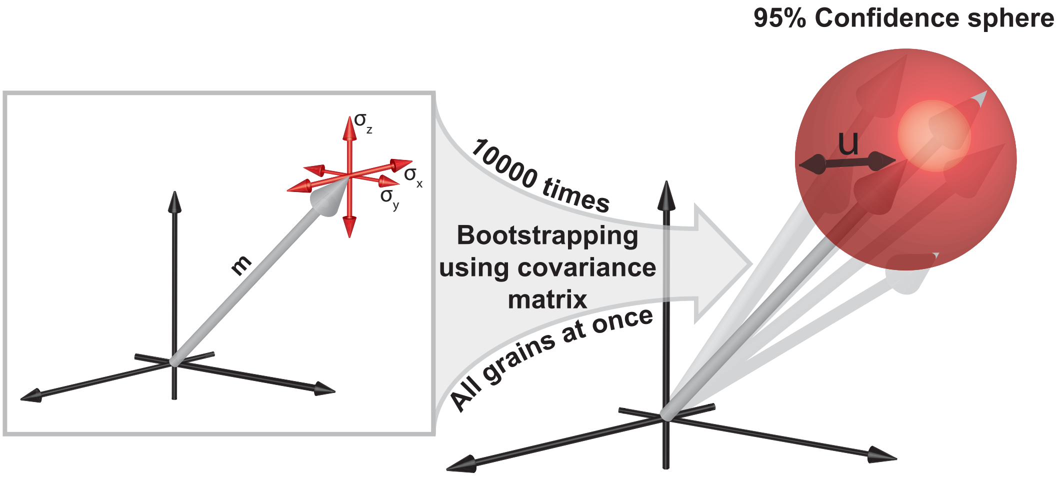


$$\text{Uncertainty Ratio} = \frac{u}{|\mathbf{M}|} \times 100\%$$

**Figure 2.** The construction of the uncertainty ratio. The covariance matrix is bootstrapped to generate a set of 10,000 possible magnetization vectors around mean magnetization vector $\mathbf{M}$. The radius of a sphere containing 9,500 of the end-points of these vectors is defined as the 95% confidence sphere with radius $u$. The length of the magnetization vector $|\mathbf{M}|$ and $u$ are then used to define the uncertainty ratio of a solution.

magnetizations per grain and per $x$, $y$, and $z$-component. Now we have found an expression for the covariance and standard deviation of the three magnetization components for individual grains. We will use these expressions in the next section to calculate the 95% confidence sphere and the uncertainty ratio.

#### *2.2.2 Calculation of the 95% confidence sphere*

The 95% confidence sphere is set-up by bootstrapping the covariance matrix and magnetization of all grains simultaneously; the radius of the sphere is determined per grain in such a way that 95% of the samples are located within the sphere. First, a multivariate normal distribution, which has as input both the total magnetization vector $\mathbf{M}_a$ and the complete covariance matrix, is sampled 10,000 times to generate 10,000 magnetization vectors for each grain at once. Then, we constructed per grain 10,000 difference vectors, which represent the difference between the bootstrapped vectors and the individual mean magnetization vector $\mathbf{M}$. The norms of these difference vectors are sorted in ascending order and the 9,500th norm value is used as radius, $r$, for a 95% confidence sphere centered at $\mathbf{M}$.

By presenting uncertainty in this way we have implicitly assumed that the bootstrapped magnetization vectors are Fisherian distributed, which means that the deviation from the mean is the same in every direction (Fisher, 1953). However, the standard deviations of magnetization are not equal in the $x$, $y$, and $z$-direction. The real distribution is probably more similar to an elliptic Kent distribution (Kent, 1982). The downside of parametrizing the Kent distribution is the necessity to use three parameters to describe an ellipsoid. Nevertheless, it depends on the type of research whether the focus is put on either uncertainties in the orientation, the norm, or both. To accommodate both sides we assume a Fisherian distribution, which can be visually represented by a 95% confidence sphere around the mean magnetization vector.

After obtaining the 95% confidence sphere, we notice that the radius of the confidence sphere is an absolute measure. This makes it difficult to compare the magnetization uncertainties of grains with different mean magnetizations. Furthermore, the magnetization solution and thus the 95% confidence sphere is dependent on the volume of the grain. Unfortunately, the grain volume is not constrained well due to measurement errors of the MicroCT. To acquire a volume independent uncertainty parameter per grain, we have defined the uncertainty ratio. The uncertainty ratio can be calculated by dividing the radius of the 95% confidence sphere, $u$, by the mean magnetization vector $|\mathbf{M}|$ per grain, which eliminates the volume dependency (Fig. 2):

$$\text{uncertainty ratio} = \frac{u}{|\mathbf{M}|} \times 100\%. \tag{12}$$

### 2.3 Signal strength ratio

The performance of the MMT technique depends on how well the magnetic moment of an individual grain is expressed in the magnetic flux map on the surface of the grain. To assess the potential maximum contribution to the magnetic flux on the surface of the sample arising from an individual grain Cortés-Ortuño et al. (2021) defined the $V/R^3$ ratio. This property is dependent on the distance of the geometric center of the grain to the scanning surface, $R$, and the volume of the grain, $V$, (see Appendix of de Groot et al., 2018). Unfortunately, the $V/R^3$ ratio does not account for the magne-

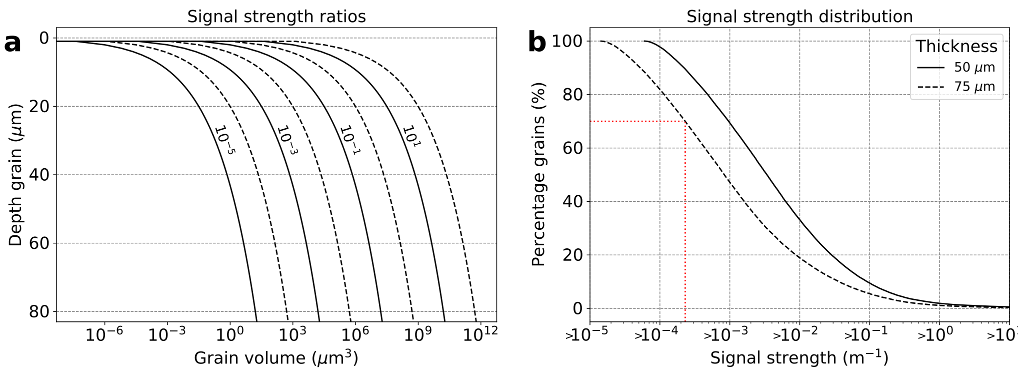


**Figure 3.** a) Relation between grain depth and grain volume as a function of SSR. b) Reversed cumulative SSR distribution for a 50 and 75 $\mu$m thick sample based on grains of the volcanic sample of de Groot et al. (2013). This panels shows, for example, that 70% of the grains in a modeled sample with a thickness of 75 $\mu$m have a SSR larger than $2.3{\times}10^{-4}$, as indicated by the red dotted lines.

tization of grains as function of their volume. Smaller SD to PSD grains have on average stronger magnetizations than larger MD grains (Dunlop, 1990; de Groot et al., 2018, 2021). de Groot et al. (2021) showed that if the diameter of a grain increases one order of magnitude, then the magnetization decreases approximately by one order of magnitude for PSD and MD grains. We already have incorporated this relation in our models using equation (1). This equation shows that the magnetization norm decreases with one order of magnitude if the volume increases by three orders of magnitude, equivalent to an increase in diameter of one order of magnitude. For this reason we have defined the signal strength ratio, SSR, as

$$\mathrm{SSR} := \frac{V}{R^3 d}, \tag{13}$$

with $d$ the diameter of the grain in $\mu$m, assuming that the volume of the grain is shaped like a sphere. Fig. 3a shows the effect of the signal strength. It shows that, although smaller grains are now parametrized to produce a stronger signal, larger signal strengths are still linked to predominantly larger grain volumes.

The cumulative distribution of the SSR per model is shown in Fig. 3b. All models use the same randomly selected grains from the volcanic sample, therefore, we only distinguished a SSR distribution for the 50 and 75 $\mu$m thick samples, since the thickness of the sample is the only factor influencing the SSR distribution. Because the 75 $\mu$m sample contains deeper grains, the minimum SSR for those models is lower than for 50 $\mu$m thick models. Approximately 70% of the grains in a 75 $\mu$m thick model have a SSR of at least $2.3 \times 10^{-4}$. This SSR is obtained, for example, for a grain with a volume of 10 $\mu$m$^3$ at a depth of 25 $\mu$m. On the other hand, 70% of the grains in a 50 $\mu$m thick model have a SSR larger than $9.8 \times 10^{-4}$. A grain with this SSR and a volume of 10 $\mu$m$^3$ would be located at a depth of 16 $\mu$m. Here, we have seen that a grain with a low SSR has more difficulty expressing its magnetic flux at the surface, but the exact relation between the grain's SSR and the uncertainty of a magnetization solution is not known and will be investigated in section 3.2.

# 3 Results

First, we present the influence from sample surface size, sample thickness, grain density, noise level, and sampling interval on the uncertainty ratio of the obtained magnetizations. Thereafter we will focus on individual magnetization solution, where we inspect the minimally needed SSR to produce magnetization results with an acceptable uncertainty ratio.

## 3.1 Uncertainty ratio

### *3.1.1 Grain density*

After running and combining results of all fifteen iterations per model, the sizes of all uncertainty ratios are sorted per noise level and summarized in Fig. 4 for the 200×200 and 500×500 $\mu$m$^2$ sample surface sizes. Per model, the distribution of the uncertainty ratio of all grains is presented in a box-plot. We indicate an uncertainty ratio of 10% as a reference size in the panels of this figure, because it is the largest uncertainty value still considered low (*e.g.*, Berndt et al., 2016). A 10% uncertainty ratio means that 9,500 of the 10,000 bootstrapped vectors are located within a sphere, which has a radius of 10% of the norm of the mean magnetization vector.

For the samples with a surface size of 500 × 500 $\mu$m and a thickness of 50 $\mu$m we observe an exponential increase in uncertainty ratio with respect to grain density (Fig. 4e-f). At least 75% of the grains in models with grain densities smaller than or equal to $10^4$ grains per mm$^3$ are associated with small uncertainty ratios (<10%), which means

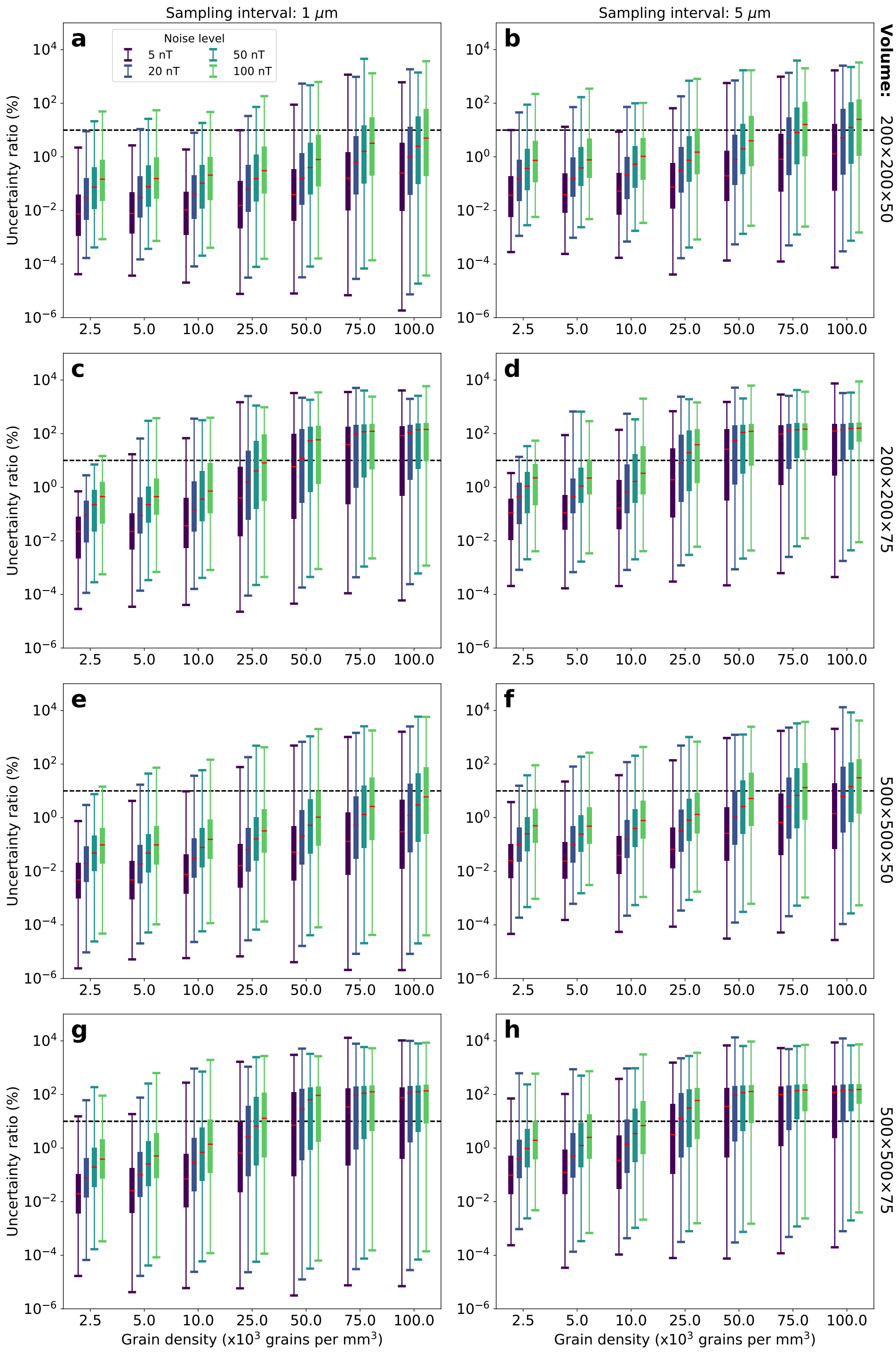


**Figure 4.** Box-plots showing per model the distribution of the uncertainty ratio of all grains as a function of grain density. The red line in each box-plot indicates the median uncertainty ratio, the bottom and top edges of the solid rectangles show the first and third quartile respectively. The bottom and top of each box-plot show the minimum and maximum uncertainty ratio respectively per model. The set of panels a-d show results for a 200×200 $\mu$m$^2$ sample surface and the set of panels e-h show results for a 500×500 $\mu$m$^2$ sample surface. Each of the four box-plots per panel per grain density correspond from left to right to one of the four noise levels, respectively 5, 20, 50, and 100 nT. The top panels of each set (a-b and e-f) refer to a 50 $\mu$m thick sample. The bottom panels of each set (c-d and g-h) refer to a sample with a thickness of 75 $\mu$m. The first column of panels is constructed with a sampling interval of 1 $\mu$m and the second column is constructed with a sampling interval of 5 $\mu$m.

that most grains in these distributions are relatively well solved. For grain density levels larger than $25 \times 10^3$ grains per mm$^3$, uncertainty ratios of about 25% of the grains exceed 100%. These large uncertainties potentially mean that some grains in volcanic samples, which have similar grain densities, cannot be resolved well. However, more than half of the grains still have uncertainty ratios smaller than 1% for the best-case scenario (i.e. instrumental noise of 5 nT, sampling interval of 1 $\mu$m). Therefore, most grains can be well solved with a sufficiently small uncertainty.

#### *3.1.2 Noise level*

Increasing the noise level from 5 to 100 nT results in an overall increase of all uncertainty ratios between one and two orders magnitude (Fig. 4e). These larger uncertainties are expected, because a larger noise level directly increases the standard deviation of the solution through the covariance matrix (see equation (11)). The median uncertainty ratio for the highest grain density increases from 0.5% to 10% for a noise level of respectively 5 and 100 nT and the smallest sampling interval, but the median uncertainty ratio for the lowest grain density increases only from 0.01% to about 1%. This shows that the noise level has more influence on the total validity of a high grain density solution than on a low grain density solution, although this trend is partly obscured by the log scale in the figures.

#### *3.1.3 Sampling interval*

The sampling interval has an exponential effect on the uncertainty ratio, which looks similar to an intensification of the noise level (Fig. 4e-f). Nevertheless, the increase becomes stagnant between a sampling interval of 4 and 5 $\mu$m, but is amplified between a sampling interval of 1 and 2 $\mu$m or 2 and 4 $\mu$m (Fig. S1a-d in Supplementary Information). This property can be attributed to the relatively smaller decrease in the number of surface magnetic scan points because the amount of points lowers by only 36% when reducing the sampling rate from 4 to 5 $\mu$m, yet the amount of points lowers by 75% when reducing the sampling interval from 1 to 2, or from 2 to 4 $\mu$m.

The effect of a decreasing sampling rate on the solution uncertainty shows that the increase in uncertainty ratio becomes progressively larger for increasing grain density. Additionally, the combination of elevated noise levels and coarser sampling rates results in median uncertainty ratios over 10% for the largest grain density (Figure 4f). This makes a majority of the grains in such samples difficult to use in subsequent interpretation stages, as the uncertainty increases substantially. However, it is premature to state that using a coarser resolution always increase uncertainty. For example, scanning a sample four times with a resolution of 2 $\mu$m results into the same uncertainty ratio as obtained when scanning a sample once using a 1 $\mu$m resolution. Additionally, the inversion is proven to be faster for lower resolution due to the smaller number of data points. On the other hand, small scale features, which might be important for solving higher order multipole moments, may not be detected using a coarser resolution.

#### *3.1.4 Sample thickness*

Sample thickness is a major factor that influences the uncertainty ratio. A comparison of panels e against g, and f against h of Fig. 4 shows that for every noise level and sampling interval scenario, the median uncertainty ratios of a majority of grains increase more than one order of magnitude when increasing the sample thickness from 50 to 75 $\mu$m. The first quartile for a grain density of $25{\times}10^3$ grains per mm$^3$ is below 10% for a 50 $\mu$m sample, but for a 75 $\mu$m sample this range is partly exceeding the 10% already for all sampling intervals. For the high grain density samples ($> 25{\times}10^3$ grains per mm$^3$) the effect of a higher sample thickness is more severe, because more than half of their grains have an uncertainty ratio of $\geq$10%. For the highest noise levels at least 50% of the grains have uncertainty ratios larger than 100%. However, low grain density samples ($< 25{\times}10^3$ grains per mm$^3$) still have a majority of grains with an uncertainty ratio <10% for every combination of noise level and sampling interval.

#### *3.1.5 Sample surface size*

The effect of the sample surface size is small compared to sample thickness. A comparison of the panels a-d and e-h of Fig. 4 indicates that the first and third quartiles of the uncertainty ratio distribution of the 75 $\mu$m samples for both domain sizes are very similar. The lowest grain densities of the 75 $\mu$m sample show somewhat lower and less scattered uncertainty ratios for the 200 $\times$ 200 $\mu$m$^2$ sample surface size than for the same sample in the 500 $\times$ 500 $\mu$m$^2$ sample surface. The uncertainty ratio distribution for the larger grain densities for both sample surfaces is on average the same. It is therefore reasonable to assume that the surface area of the sample does not play a major role in determining correct grain magnetizations for most grain densities, because the extra unknown grain magnetizations are balanced by the data from the increased amount of flux sensors at the top of the sample. The only downside of using a large sample surface size is the increased amount of computational power needed to solve the inversion, since the Green's matrix expands linearly for the number of grains, and expands squarely for the number of sensors.

### 3.2 Signal strength ratio

Up to this point the distribution of the uncertainty ratios for combinations of different grain densities, noise levels, sampling intervals, sample thicknesses, and sample surface sizes have been assessed. From the results we observe that for samples with high uncertainty (*e.g.* 75 $\mu$m thickness and high grain density) it is possible to find small groups of grains with very low uncertainty ratios ($< 10\%$). To determine which grains in a certain model produce acceptable uncertainties, we assess the SSRs as function of the uncertainty ratios of the magnetizations. In Fig. 5 the minimally needed SSR to solve the magnetization of 99% of the grains with a certain uncertainty ratio is plotted as function of grain density in the models with a sample surface size of $500 \times 500$ $\mu$m$^2$. Each panel in the figure contains five uncertainty ratios, namely, 1%, 3%, 5%, 10%, and 20%.

Panel a of Fig. 5 shows that up to a grain density of $10^4$ grains per mm$^3$ in a sample with a thickness of 50 $\mu$m, SSRs of $6.7 \times 10^{-5}$ can be solved within uncertainty ratios as small as 10% for a low noise level and a high sampling resolution. This means, for example, that grains with a volume of 10 $\mu$m$^3$ can be solved with an uncertainty ratio of at least 10% at a maximum depth of 38 $\mu$m. However Fig. 5b shows that for the worst possible conditions, *i.e.* a noise level of 100 nT and a sampling rate of 5 $\mu$m, only grains with a SSR of $2.4 \times 10^{-3}$ can be solved at 10% uncertainty ratio, which corresponds to solving a 10 $\mu$m$^3$ volume grain at 12 $\mu$m depth. According to Fig. 3b, about 55% of the grains have a SSR equal to or larger than $2.4 \times 10^{-3}$.

The 99% resolved SSR is rising quickly for grain densities higher than $10^4$ grains per mm$^3$. For the largest grain density and best-case scenario, *i.e.* a noise level of 5 nT and a sampling rate of 1 $\mu$m, SSRs larger than $3.4 \times 10^{-3}$ can be solved within an uncertainty ratio of 10%. This SSR corresponds to solving about 50% of total amount of the grains. In a worst-case scenario grains with a SSR larger than $2.9 \times 10^{-2}$ can be solved

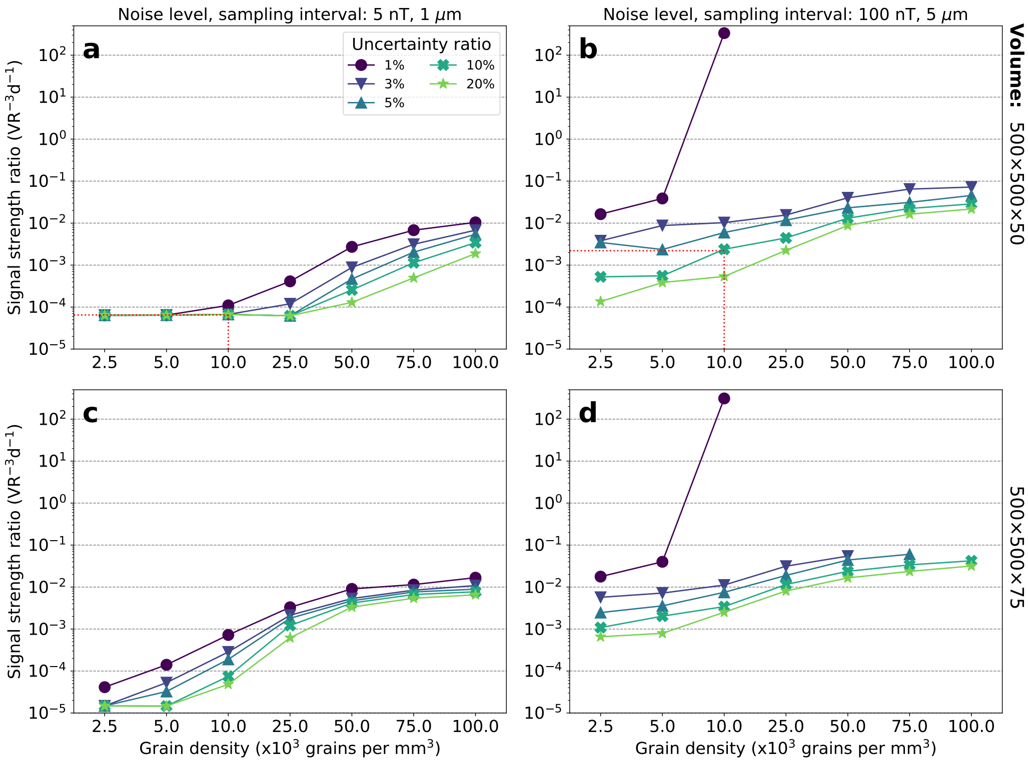


**Figure 5.** SSR resolved at 99% criterion, plotted against grain density for different uncertainty ratios for the 500×500 $\mu$m$^2$ sample surface. The top row of panels is obtained for a sample thickness of 50 $\mu$m. The bottom row of panels is based on a sample thickness of 75 $\mu$m. Panels a and c represent results for a noise level of 5 nT and sampling interval of 1 $\mu$m. Panels b and d show results for a noise level of 100 nT and sampling interval of 5 $\mu$m. Each panel contains five lines corresponding to different uncertainty ratios, namely, 1% (circle), 3% (upper base triangle), 5% (lower base triangle), 10% (cross), and 20% (star). The red dotted lines in panel a and b represent an example described in section 3.2, which shows that the SSR increases from $7 \times 10^{-5}$ to $10^{-2}$ when experimental conditions deteriorate for a sample with a grain density of $10^4$ grains per mm$^3$ and 10% uncertainty ratio. These signal strengths corresponds to, *e.g.*, solving a 10 $\mu$m$^3$ grain at a depth of 38 and 7 $\mu$m, respectively. Some points are missing because no SSR could be found for cases where 99% of the grains pass the uncertainty criterion.

for the same grain density and uncertainty ratio. For both scenarios only grains close to the sample surface produce a SSR large enough to be properly solved.

The sample thickness is again a major factor determining the minimally needed SSR to solve grains for a given uncertainty ratio as shown by the panels c-d of Fig. 5. Especially the influence on small grain densities for the lowest noise levels and sampling intervals is large. Only for an uncertainty ratio larger than 1% can all grains be solved for the smallest grain density. Furthermore, the larger grain densities contain few grains that can be solved for the highest noise level and sampling interval. For the smallest uncertainty ratios of 1% and 3% there are no SSRs for which 99% of the grains are solved. Nevertheless, comparing panels a-b against c-d in Fig. 5 shows that the minimum SSR of the larger grain densities for the same noise level and sampling interval scenario does not change significantly. This means that a thicker sample does not increase the minimally needed SSR to solve a grain for a given uncertainty ratio, implying that shallow grains are not solved worse due to distortion of the weak signal of deep grains. The reason for solving less grains in thicker samples is, therefore, that less grains have, relatively, the minimally needed SSR, which is caused by a changed SSR distribution as shown by Fig. 3b.

Decreasing the sample surface size causes minor changes in resolved SSR for both sample thicknesses (see Supplementary Figs. S5 and S6). The SSR of smaller grain densities decreased the most. This decrease in SSR makes it more likely for samples with grain densities up to $10^4$ grains per $mm^3$ to obtain confidence sphere sizes lower than 10%, even for high noise levels and coarse sampling rates.

# 4 Discussion

## 4.1 Parameter impact on uncertainty

We set up a range of numerical models to investigate the responses of grain density, sampling interval, noise level, sample surface size, and sample thickness on the uncertainty of magnetization solutions. Additionally, we assess which combinations of depth and grain size provide stable results given the changing initial conditions. The overall results indicate that the quality of the solutions is highly dependent on grain density in the sample. The grain density directly increases the amount of variables in the inversion, which leads to an increase in condition number and, therefore, in uncertainties. The grain density enlarges the uncertainty ratio distribution up to four orders of magnitude from the best to the worst case scenario in our models. The uncertainty ratio raises rapidly for grain densities larger than $10 \times 10^3$ grains per mm$^3$.

The effect of noise level and sampling interval on magnetization uncertainty is similar, because they both affect the uncertainty ratio with an increase of up to two orders of magnitude. Compared to the influence of grain density, however, we perceive the effect of noise level and sampling rate to be less severe over the magnetization uncertainty. The noise level does not have a significant influence because the surface magnetic field has, on average, a strength in the order of $10^{-6}$ to $10^{-3}$ T, which is many times larger than the largest realistic noise level of 100 nT (Glenn et al., 2017). In the case of sampling interval, its limited influence can be attributed to the vastly overdetermined inversion system, considering that the system contains at least twice as many knowns than unknowns. Moreover, these two parameters can be directly controlled during the experimental set-up, hence the noise level and sampling interval can be further minimized when needed.

The sample surface size has the smallest effect on the magnetization uncertainty of all parameters tested here, because it does not change the ratio of known magnetic field data and unknown magnetization variables in the inversion. Nevertheless, results show that the smallest grain densities obtain slightly better solutions in smaller domain areas, which can only be attributed to the presence of less unknown magnetization variables in the corresponding inversion.

Sample thickness has a major influence on magnetization uncertainty; the uncertainty can rise up to two orders of magnitude by increasing the sample thickness from 50 to 75 $\mu$m. This rise is partly caused by the SSR that quickly becomes lower for the additional deeper grains in the thicker sample (see Fig. 3b). We suggest, therefore, that the distance between sample and sensor should be as small as possible to retrieve the strongest possible signals. This leads to relatively high SSRs, resulting into signals that are well visible above the noise.

### 4.2 Implications for uncertainties in previous MMT studies

In the study of de Groot et al. (2018) MMT was used for the first time to successfully obtain individual magnetizations while making use of scanning SQUID microscopy

(SSM). They inverted magnetic signals from three subdomains in a synthetically created sample with low grain density, but without providing confidence limits for the solutions. The accuracy of the obtained magnetization solutions is hence unknown. With the results obtained here, the uncertainties of these magnetization solutions can finally be estimated.

The study focused on solving the magnetization of grains in three subdomains with an average area of 300×300 $\mu$m$^2$, a thickness of 50 $\mu$m, and an average grain density close to 2500 grains per mm$^3$. The sampling interval is 1 $\mu$m and the height of the SSM sensor above the samples is 1-2 $\mu$m. The noise level of the magnetic field produced by SSM is estimated to be much lower than 5 nT, although positional noise can further increase the noise level (Weiss et al., 2007; Lee et al., 2004). We combined the provided information with the newly acquired results of section 3.2. Based on the assumption that we approximately have a 200×200 $\mu$m$^2$ sample surface with a thickness of 50 $\mu$m for compatibility, we conclude that the uncertainty ratios of the grains in the study were much smaller than 1% (see Fig. 4a). In the extreme case that positional noise would increase the noise level to an unrealistically high level of 100 nT, grains with a SSR larger $9.7\times10^{-4}$ could still be solved with uncertainty ratios of 1%, which is about 70% of the total amount of grains (see Supplementary Information Fig. S5d). The effect of the additional distance of 1-2 $\mu$m between sample and scanning sensor is not significant, considering that the comparison of panels a and c of Fig. 5 show almost no difference in the minimally needed signal strength to solve a grain with an uncertainty ratio of 1% for a density of 2500 grains per mm$^3$. In conclusion, the magnetization results in de Groot et al. (2018) were obtained with high precision.

### 4.3 Convergence of model results

Although the models have been iterated fifteen times, variations caused by model specific configurations can still persist in the obtained uncertainty ratios and distribution or SSRs. The variations in the uncertainty ratio distribution (Fig. 4) have been estimated by comparing the change in cumulative uncertainty ratio distribution each time after a model has been run. The change in median declines, on average, from 80% after two iterations to less than 5% after fifteen iterations. Extending the amount of iterations appears to have no effect, as the average deviation remains around 5% and does not show a declining trend. The lowest grain densities show the highest deviations in median uncertainty ratio of up to 15%, probably because the confidence interval is averaged over less grains compared to denser samples.

The SSR distribution exhibits deviations of a quarter of a log scale after fifteen iterations for most sampling intervals, noise levels, and sample thicknesses. The SSR associated with the lowest grain densities can change more than half an order in magnitude, contrary to denser samples that change on average less than a quarter of an order magnitude. Similarly to the uncertainty ratio distribution, lower grain densities have more difficulty to produce a constant signal strength average over the model iterations, because they have less grains to cover all positions in the model within fifteen iterations. It is possible that increasing the number of iterations of the model can improve the convergence of the SSRs of grains with lower grain densities. On the other hand, low grain densities have on average a lower minimal SSR and initially a higher percentage grains that pass the uncertainty ratio. Therefore, an error of a quarter of magnitude that is introduced here will not increase the uncertainty ratio of the majority of the grains such that they become unusable for further analysis. The estimated errors for the higher grain densities, likewise, have little effect on the percentage of grains that can be solved, because the potential raise in minimally needed SSR will only result in the rejection of a very small percentage of grains (see Fig. 5).

### 4.4 Setting a SSR threshold

The SSR is a powerful statistic to quickly discriminate between grains that are resolved well by the MMT inversion and grains that are not properly resolved. For each MMT inversion it is important to set a useful threshold for the SSR for the specific purpose of a study. This threshold depends on the five parameters of the inversions as studied here, and on the required accuracy of the accepted magnetizations. The SSR threshold needs to be balanced between rejecting grains with an accurate solution that do not meet the SSR criterion and including grains that do fulfil the SSR requirements, but are not properly resolved by the inversion. In Fig. 6 we illustrate this based on all grains in the models with dimensions $500\times500\times50$ $\mu$m, a grain density of $10^5$ grains per mm$^3$, sampling interval in the magnetic scan of 1 $\mu$m, and a magnetic noise level of 5 nT. We once again accept a magnetization solution as accurate if the uncertainty ratio is <10%. In total there are 18,750 grains in these models, of which 15,301 grains have uncertainty ratios <10%; they would ideally be selected as the accurate subset of grains. We deter-

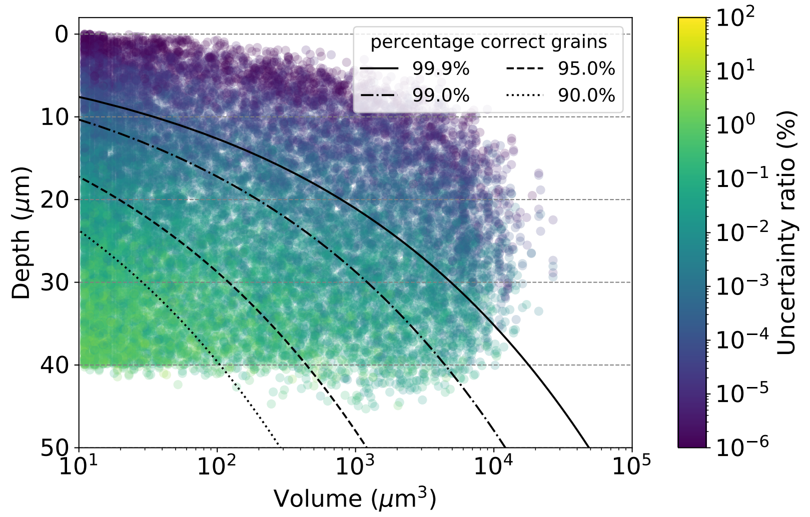


**Figure 6.** Using the SSR to select subsets of grains with accurately resolved magnetizations for our models with a grain density of $10^5$ grains per mm$^3$, sampling interval of 1 $\mu$m, and noise level of 5 nT for a 500 $\times$ 500 $\times$ 50 $\mu$m sample surface. The grains are colored according to their uncertainty ratio. Four different SSRs select 99.9, 99.0, 95.0, and 90.0% of the grains with an uncertainty ratio of maximum 10%.

mined SSRs to select sets of grains for which 90.0, 95.0, 99.0, and 99.9% of all accepted grains have an uncertainty ratio <10%. When 99.9% of the grains in the subset must fulfill the uncertainty ratio criterion, 6,565 grains are selected using a SSR of $8.6\times10^{-3}$, i.e. only 42.9% of the desired grains are selected. When 1% of the grains are allowed to violate the uncertainty ratio criterion, the number of grains in the subset increases to 9,342, but 93 of these violate the uncertainty ratio criterion, so 58.0% of the desired grains are recovered by the SSR of $3.4\times10^{-3}$. For the case where 95% of the grains is allowed to have an uncertainty ratio <10%, the SSR of $7.3\times10^{-4}$ accepts 13,863 grains. This implies that although there are 693 grains in this subset that violate the uncertainty ratio criterion, 86.1% of all desired grains are accepted. When 10% badly resolved grains are accepted, 16,289 grains pass the SSR selection of $2.8\times10^{-4}$, and 95.8% of all properly resolved grains pass, although also 1,629 grains that violate the uncertainty ratio criterion are accepted as well.

The SSR to select a set of accurately resolved grains can be estimated for inversions with different parameters by running computational models with these specific sample dimensions and magnetic scan parameters. Running these additional computational models to determine the best SSR for a specific MMT inversion and purpose of course takes some time, but it is currently the only way to select the most reliable subset of grains after an inversion in a objective way. Moreover, these computational models can also be analyzed before the actual MMT experiments are done based on the parameters that are difficult to control during the experiments (*e.g.* the grain density of the sample). This can help to determine to optimal sample dimensions and boundary conditions for the magnetic surface scans for the MMT experiments.

### 4.5 A preliminary assessment of empirical uncertainties

Here we studied the mathematical accuracy and performance of MMT inversions by running simulations with varying boundary conditions. We proposed and assessed new statistical parameters to scrutinize MMT results that allow to select the magnetic moments of only well resolved grains. This theoretical framework will also aid solving the empirical challenges that the development of MMT still faces. A prerequisite for MMT, for example, is that all surface magnetic signals within a domain belong to grains within that same domain (Fabian & De Groot, 2019). This condition is often violated in MMT studies on natural samples because a proportion of small magnetic sources in samples are undoubtedly missed due to the resolution limits of the MicroCT experiments (de Groot et al., 2021). The currently used MicroCT analyses have resolutions $>0.7$ $\mu$m and inherently miss smaller grains. Small PSD and SD grains, therefore, remain undetected in natural samples even though they may produce a signal in the surface magnetic map. A comprehensive study on the impact of errors in the MicroCT analyses is currently an ongoing project but here we provide a preliminary assessment of the effect of missing grains.

We set up and inverted 15 models which also contain grains smaller than 1 $\mu$m$^3$. To obtain a realistic amount of small grains, a grain diameter distribution was defined by fitting a log-normal distribution to the MicroCT data described in section 2.1.1 to populate our models (Yu et al., 2002; Smirnov, 2006). This distribution was created in SciPy (Virtanen et al., 2020) using the parameters scale = 0.9, shape = 0.9, and location = 0.0. Then this distribution was sampled to obtain approximately 550 spherical grains of which 200 grains have a volume larger than 1 $\mu$m$^3$. All grains were assigned a magnetization according to equation 1 and were randomly placed in a $200\times200\times50$ $\mu$m$^3$ domain without intersecting other grains. A forward field was obtained with a sampling interval of 1 $\mu$m and a noise level of 5 nT. Grains smaller than 1 $\mu$m$^3$ were then removed before the MMT inversion, simulating missing grains in the MicroCT analysis. The remaining 200 grains, which represent a grain density of $10^5$ grains per mm$^3$, were inverted and their relative magnetization error was assessed as function of SSR.

For this configuration, without missing grains, a SSR of $2 \times 10^{-3}$ was sufficient to solve 99% of the grains with an uncertainty level of 10%, according to our SSR analysis in section 3.2 (Figure S5a). However, the results obtained when grains are missed by the MicroCT show that a SSR of approximately $10^{-1}$ is required to obtain a relative magnetization error of 10% for 99% of the grains in the inversion. We observe that this occurs independent of noise level, sampling interval, grain density, and domain size, indicating that every grain would require a SSR of $10^{-1}$ when a MicroCT with 1 $\mu$m resolution is used. Remarkably, even in the present very unfavourable scenario MMT is still capable of producing accurate results for both large and shallow grains in the sample. Given the preliminary nature of these results we must remark that to fully quantify the impact of the effect of missing grains by MicroCT analysis on MMT results it is required to do a focused future in-depth study.

### 4.6 Limitations and future research

This modeling study is the first attempt to quantify errors associated with individual magnetization solutions as produced by MMT. We have made, therefore, some simplifying assumptions. First of all, we assumed uniform magnetization sources for all grains. Most natural grains will not have a uniform magnetization structure, but a more complex magnetic structure best represented by a multipolar approximation (Butler, 1992; Cortés-Ortuño et al., 2021). This complex structure could introduce additional uncertainties in the inversion, since the sensitivity to noise of quadrupole, octupole, and higher order magnetization terms is currently unknown. However, results from Cortés-Ortuño et al. (2021) show that the solved dipolar magnetization changes when multipole terms are added to the calculation. Also the amount of variables to solve per grain increases when solving for multipole terms, while the amount of data points in the magnetic surface scan does not increase. Therefore, it would be worthwhile to investigate the sensitivity of these higher order multipole terms to noise, and to study the effect of adding these higher order terms on the uncertainty of the total solution. Fortunately, the magnetic response of multi-domain grains quickly declines with increasing depth, hence we would solely need to model multi-domain grains until a depth of 10 to 20 $\mu$m (Cortés-Ortuño et al., 2021).

Furthermore, we assumed that the noise in the magnetic field scan is Gaussian distributed. This assumption is incorrect for natural samples for a couple of reasons. First of all, most grains have a complex multi-domain magnetization structure, but they are solved as if they were in a uniform state. This means that residuals caused by unsolved higher order magnetic moments will introduce correlated noise to the magnetic surface field. This problem can be approached by using a computational code that allows for solving higher order multipole moments (Cortés-Ortuño et al., 2021).

Another problem that persists within MMT is the limited amount of grains we can invert for at once. Computationally, we can now run an MMT inversion for a sample of $500 \times 500 \times 75$ $\mu$m and a grain density of $10^5$ grains per mm$^3$. This requires a computational system with 52 cores and 192 GB of RAM, which enables us to invert for almost 2000 grains at once. Currently, the main limitation for the inversion of larger samples is the RAM capacity of the machine. The RAM requirements can be lowered in the future with further optimizations to the numerical code (e.g. Kabir et al., 2017). Alternatively, it is also possible to reduce the resolution of the scanning grid or reduce the amount of variables by grouping grains when solutions, according to the covariance matrix, are strongly correlated and consequently have a high individual uncertainty ratio. Although this does not decrease the number of data points at the surface, the uncertainty of the grouped grains is improved and the amount of variables is reduced. Another option is to invert smaller subdomain regions that can be handled by the computational system. Nonetheless, problems will arise in consistency of the magnetization solution of grains near the boundaries of the subdomains, because the subdomains are likely magnetically joint, thereby violating the assumption of magnetic independent regions (Fabian & De Groot, 2019). Nevertheless, the inner grains of the subdomains might still have reliable solutions as long as sufficient information on their produced magnetic surface field is available in the subdomain. An option is to use a thicker sample, which will immediately increase the number of grains without changing the amount of data points in the magnetic surface scan. However, we have shown that increasing the sample thickness leads to a significant increase in uncertainty ratio, because the deeper grains have an insufficient signal strength to be noticeable at the surface.

### 4.7 Paleomagnetic outlook

One of the ultimate aims of Micromagnetic Tomography studies is to derive paleomagnetic interpretations, i.e. paleodirections and paleointensities, from subsets of grains in a sample. In our study we assigned the magnetizations of our grains randomly. Therefore an interpretation of the magnetic moment of the entire sample of subsets of grains in our model is meaningless. Nevertheless, future MMT studies could obtain a total magnetic moment vector of a real sample by plotting the magnetic moment solutions and respective uncertainties of each grain on a polar plot. Then by applying appropriate statistics (e.g. Fisher, 1953; Kent, 1982) an estimate of the total magnetic moment vector of a sample can be obtained. Conclusions about paleointensities are even harder to obtain. As shown by Berndt et al. (2016), at least 10 million small SD grains are required to obtain a proper estimation of the paleomagnetic field. But it is currently unknown under which conditions larger, PSD or MD, grains may provide valuable paleomagnetic information; and if so, how many of these grains would be sufficient for a reliable interpretation of paleodirections and/or paleointensities. Recently, PSD grains receive increasingly more attention as reliable paleomagnetic recorders. For example, Nagy et al. (2017) suggests that grains with diameters up to 1 $\mu$m are capable of retaining stable magnetizations of geologic timescales. Solving for the magnetization of PSD grains using MMT is currently still challenging since most MicroCTs cannot completely detect grains $< 1$ $\mu$m, creating errors in the magnetic moments (see Section 4.5). The MicroCT scans for ongoing MMT studies, however, attain resolutions $< 500$ nm, implying that the detection of large PSD grains is within technological reach. Given the technological developments in MicroCT scanners combined with the rapidly maturing MMT inversion technique, we believe that MMT will be a valuable asset in the paleomagnetic toolbox in the near future.

## 5 Conclusions

In this study we have acquired a first order estimation of the uncertainties of individual magnetization solutions using MMT. With the help of numerical models we showed that grain density and sample thickness are the major factors influencing the mathematical uncertainty of the magnetization solutions. Noise level and sampling interval are of secondary importance, because these parameters are controllable during experiments.

The sample surface size minimally influences the results and should only be decreased when the size of the surface magnetic scan leads to overflowing computer memory.

Using the SSR as defined in this study helps to identify individual grains with an accurate magnetic solution as indicated by a low uncertainty ratio, even when a specific combination of the investigated parameters (grain density, noise level, sampling interval, sample surface size, and sample thickness) pose a challenge to the MMT inversion. The SSR is based on volume and depth of a grain, hence it is not necessary to rerun the inversion to obtain individual uncertainty levels through the covariance matrix. The thresholds for the SSR obtained in this study can, therefore, be applied to other MMT studies that involve the same inversion procedure. In this way we can extract individual well-resolved grains from overall challenging samples and obtain an accurate magnetic moment solution from only those grains.

We verified that the results for uncertainty ratio distribution and SSR converge within fifteen model iterations. Nevertheless, the stability of magnetization results can degrade due to undetected grains in the MicroCT scan. Through the ongoing development of MicroCT, this challenge will eventually be solved for. Additionally, errors caused by incorrectly solving shallow multi-domain grains using the dipole assumption might influence the solution, but this source of error can be controlled by employing the multipole method of Cortés-Ortuño et al. (2021). In this context, modelling shallow grains with higher order magnetic moments will allow to observe the effect of higher order terms on the uncertainty of the individual magnetization solutions in a future study. In summary, by analyzing the effect of five strongly influencing parameters in MMT experiments we have provided a first framework to quantify the uncertainties of the magnetization solutions of natural magnetic grain samples. Consequently, these results can be applied to further paleomagnetic studies to determine the accuracy of obtained natural remanent magnetizations and to individually select reliable grains from bad samples.

## Acknowledgments

Numerical calculations were executed with support of NumPy (Harris et al., 2020), SciPy (Virtanen et al., 2020), and Matplotlib (Hunter, 2007) Python libraries. This project has received funding from the European Research Council (ERC) under the European Union's Horizon 2020 research and innovation program (Grant agreement No. 851460 to L.V. de Groot).

## References


Berndt, T., Muxworthy, A. R., & Fabian, K. (2016, 1). Does size matter? Statistical limits of paleomagnetic field reconstruction from small rock specimens. *Journal of Geophysical Research: Solid Earth*, *121*(1), 15–26. Retrieved from https://onlinelibrary.wiley.com/doi/10.1002/2015JB012441 doi: 10.1002/2015JB012441

Butler, R. F. (1992). *PALEOMAGNETISM: Magnetic Domains to Geologic Terranes.* Boston: Blackwell Scientific Publications.

Cortés-Ortuño, D., Fabian, K., & de Groot, L. V. (2021, 4). Single Particle Multipole Expansions From Micromagnetic Tomography. *Geochemistry, Geophysics, Geosystems*, *22*(4), 7031. Retrieved from http://arxiv.org/abs/2101.07010https://onlinelibrary.wiley.com/doi/10.1029/2021GC009663http://dx.doi.org/10.1029/2021GC009663 doi: 10.1029/2021GC009663

de Groot, L. V., Biggin, A. J., Dekkers, M. J., Langereis, C. G., & Herrero-Bervera, E. (2013, 12). Rapid regional perturbations to the recent global geomagnetic decay revealed by a new Hawaiian record. *Nature Communications*, *4*(1), 2727. Retrieved from www.nature.com/naturecommunicationshttp://www.nature.com/articles/ncomms3727 doi: 10.1038/ncomms3727

de Groot, L. V., Fabian, K., Béguin, A., Kosters, M., Cortés-Ortuño, D., Fu, R., ... Barnhoorn, A. (2021). Micromagnetic Tomography for Paleomagnetism and Rock-Magnetism. *Earth and Space Science Open Archive*, 44. Retrieved from https://doi.org/10.1002/essoar.10507913.1 doi: 10.1002/essoar.10507913.1

de Groot, L. V., Fabian, K., Béguin, A., Reith, P., Barnhoorn, A., & Hilgenkamp, H. (2018, 4). Determining Individual Particle Magnetizations in Assemblages of Micrograins. *Geophysical Research Letters*, *45*(7), 2995–3000. Retrieved from https://onlinelibrary.wiley.com/doi/abs/10.1002/2017GL076634 doi: 10.1002/2017GL076634

Dunlop, D. J. (1990, 6). Developments in rock magnetism. *Reports on Progress in Physics*, *53*(6), 707–792. Retrieved from https://www.researchgate.net/publication/231090758https://iopscience.iop.org/article/10.1088/0034-4885/53/6/002 doi: 10.1088/0034-4885/53/6/002

Dunlop, D. J., & Özdemir, Ö. (1997). *Rock Magnetism.* Cambridge University Press. Retrieved from `https://www.cambridge.org/core/product/identifier/9780511612794/type/book` doi: 10.1017/cbo9780511612794

Egli, R., & Heller, F. (2000). *High-resolution imaging using a high-Tc superconducting quantum interference device (SQUID) magnetometer* (Vol. 105; Tech. Rep.). doi: 10.1029/2000JB900192

Fabian, K. (2000). Acquisition of thermoremanent magnetization in weak magnetic fields. *Geophysical Journal International*, *142*(2), 478-486. doi: 10.1046/j.1365-246x.2000.00167.x

Fabian, K. (2001). A theoretical treatment of paleointensity determination experiments on rocks containing pseudo-single or multi domain magnetic particles. *Earth and Planetary Science Letters*, *188*(1-2), 45-58. doi: 10.1016/S0012-821X(01)00313-2

Fabian, K., & De Groot, L. V. (2019, 2). A uniqueness theorem for tomography-assisted potential-field inversion. *Geophysical Journal International*, *216*(2), 760–766. Retrieved from `http://arxiv.org/abs/1712.06136https://academic.oup.com/gji/article/216/2/760/5151336` doi: 10.1093/gji/ggy455

Farchi, E., Ebert, Y., Farfurnik, D., Haim, G., Shaar, R., & Bar-Gill, N. (2017, 9). Quantitative Vectorial Magnetic Imaging of Multi-Domain Rock Forming Minerals Using Nitrogen-Vacancy Centers in Diamond. *SPIN*, *7*(3). doi: 10.1142/S201032471740015X

Fisher, R. (1953, 5). Dispersion on a Sphere. *Proceedings of the Royal Society A: Mathematical, Physical and Engineering Sciences*, *217*(1130), 295–305. Retrieved from `https://royalsocietypublishing.org/doi/abs/10.1098/rspa.1953.0064` doi: 10.1098/rspa.1953.0064

Glenn, D. R., Fu, R. R., Kehayias, P., Le Sage, D., Lima, E. A., Weiss, B. P., & Walsworth, R. L. (2017, 8). Micrometer-scale magnetic imaging of geological samples using a quantum diamond microscope. *Geochemistry, Geophysics, Geosystems*, *18*(8), 3254–3267. Retrieved from `https://onlinelibrary.wiley.com/doi/abs/10.1002/2017GC006946` doi: 10.1002/2017GC006946

Harris, C. R., Millman, K. J., van der Walt, S. J., Gommers, R., Virtanen, P., Cournapeau, D., . . . Oliphant, T. E. (2020, 9). Array programming with NumPy.

*Nature*, *585*(7825), 357–362. Retrieved from http://www.nature.com/articles/s41586-020-2649-2 doi: 10.1038/s41586-020-2649-2

Hunter, J. D. (2007, 5). Matplotlib: A 2D Graphics Environment. *Computing in Science & Engineering*, *9*(3), 90–95. Retrieved from http://nipy.scipy.http://ieeexplore.ieee.org/document/4160265/ doi: 10.1109/MCSE.2007.55

Kabir, K., Haidar, A., Tomov, S., Bouteiller, A., & Dongarra, J. (2017). A framework for out of memory svd algorithms. In J. M. Kunkel, R. Yokota, P. Balaji, & D. Keyes (Eds.), *High performance computing* (pp. 158–178). Cham: Springer International Publishing.

Kent, J. T. (1982, 9). The Fisher-Bingham Distribution on the Sphere. *Journal of the Royal Statistical Society: Series B (Methodological)*, *44*(1), 71–80. Retrieved from http://doi.wiley.com/10.1111/j.2517-6161.1982.tb01189.x doi: 10.1111/j.2517-6161.1982.tb01189.x

Lee, S.-Y., Matthews, J., & Wellstood, F. C. (2004, 6). Position noise in scanning superconducting quantum interference device microscopy. *Applied Physics Letters*, *84*(24), 5001–5003. Retrieved from http://aip.scitation.org/doi/10.1063/1.1763215 doi: 10.1063/1.1763215

Nagy, L., Williams, W., Muxworthy, A. R., Fabian, K., Almeida, T. P., Conbhui, P. O., & Shcherbakov, V. P. (2017). Stability of equidimensional pseudo-single-domain magnetite over billion-year timescales. *Proceedings of the National Academy of Sciences of the United States of America*, *114*(39), 10356-10360. doi: 10.1073/pnas.1708344114

Néel, L. (1955, 4). Some theoretical aspects of rock-magnetism. *Advances in Physics*, *4*(14), 191–243. Retrieved from https://www.tandfonline.com/doi/abs/10.1080/00018735500101204http://www.tandfonline.com/doi/abs/10.1080/00018735500101204 doi: 10.1080/00018735500101204

Panovska, S., Korte, M., & Constable, C. G. (2019). One hundred thousand years of geomagnetic field evolution. *Reviews of Geophysics*, *57*(4), 1289-1337. doi: https://doi.org/10.1029/2019RG000656

Pavón-Carrasco, F. J., Campuzano, S. A., Rivero-Montero, M., Molina-Cardín, A., Gómez-Paccard, M., & Osete, M. L. (2021). Scha.dif.4k: 4,000 years of paleomagnetic reconstruction for europe and its application for dating.

*Journal of Geophysical Research: Solid Earth*, *126*(3), e2020JB021237. doi: https://doi.org/10.1029/2020JB021237

Sim, J., & Reid, N. (1999, 2). Statistical Inference by Confidence Intervals: Issues of Interpretation and Utilization. *Physical Therapy*, *79*(2), 186–195. Retrieved from `https://academic.oup.com/ptj/article/79/2/186/2837119` doi: 10.1093/ptj/79.2.186

Smirnov, A. (2006). Memory of the magnetic field applied during cooling in the low-temperature phase of magnetite: Grain size dependence. *Journal of Geophysical Research: Solid Earth*, *111*(B12).

Snieder, R., & Trampert, J. (1999). Inverse Problems in Geophysics. In *Signal recovery and synthesis* (pp. 119–190). Washington, D.C.: OSA. Retrieved from `https://www.osapublishing.org/abstract.cfm?URI=SRS-2001-SMA2http://link.springer.com/10.1007/978-3-7091-2486-4_3` doi: 10.1007/978-3-7091-2486-4{_}3

Tauxe, L., & Yamazaki, T. (2015). Paleointensities. In *Treatise on geophysics* (pp. 461–509). Elsevier. doi: 10.1016/B978-0-444-53802-4.00107-X

ter Maat, G. W., Pennock, G. M., & de Groot, L. V. (2018). Data descriptor: A chemical, crystallographic and magnetic characterisation of individual iron-oxide grains in Hawaiian lavas. *Scientific Data*, *5*, 1–9. doi: 10.1038/sdata.2018.162

Virtanen, P., Gommers, R., Oliphant, T. E., Haberland, M., Reddy, T., Cournapeau, D., ... van Mulbregt, P. (2020, 3). SciPy 1.0: fundamental algorithms for scientific computing in Python. *Nature Methods*, *17*(3), 261–272. Retrieved from `https://doi.org/10.1038/s41592-019-0686-2http://www.nature.com/articles/s41592-019-0686-2` doi: 10.1038/s41592-019-0686-2

Weiss, B. P., Lima, E. A., Fong, L. E., & Baudenbacher, F. J. (2007, 9). Paleomagnetic analysis using SQUID microscopy. *Journal of Geophysical Research*, *112*(B9), B09105. Retrieved from `http://doi.wiley.com/10.1029/2007JB004940` doi: 10.1029/2007JB004940

Yu, Y., Dunlop, D. J., & Özdemir, Ö. (2002). Partial anhysteretic remanent magnetization in magnetite 1. additivity. *Journal of Geophysical Research: Solid Earth*, *107*(B10), EPM–7.

# Supporting Information for "A first-order statistical exploration of the mathematical limits of Micromagnetic Tomography"

Frenk Out[1], David Cortés-Ortũno[1], Karl Fabian[2], Tristan van Leeuwen[3,4],

Lennart V. de Groot[1]

[1]Paleomagnetic laboratory Fort Hoofddijk, Department of Earth Sciences, Utrecht University, Budapestlaan 17, 3584 CD Utrecht, The Netherlands.

[2]Norwegian University of Science and Technology (NTNU), S. P. Andersens veg 15a, 7031 Trondheim, Norway

[3]Mathematical Institute, Faculty of Sciences, Utrecht University, Utrecht, The Netherlands

[4]Department of Computational Imaging, Centrum Wiskunde & Informatica (CWI), The Netherlands

Corresponding author: F. Out, Paleomagnetic laboratory Fort Hoofddijk, Department of Earth Sciences, Utrecht University, Budapestlaan 17, 3584 CD Utrecht, The Netherlands. (f.out@uu.nl)

# 1. Extra figures uncertainty ratio distribution

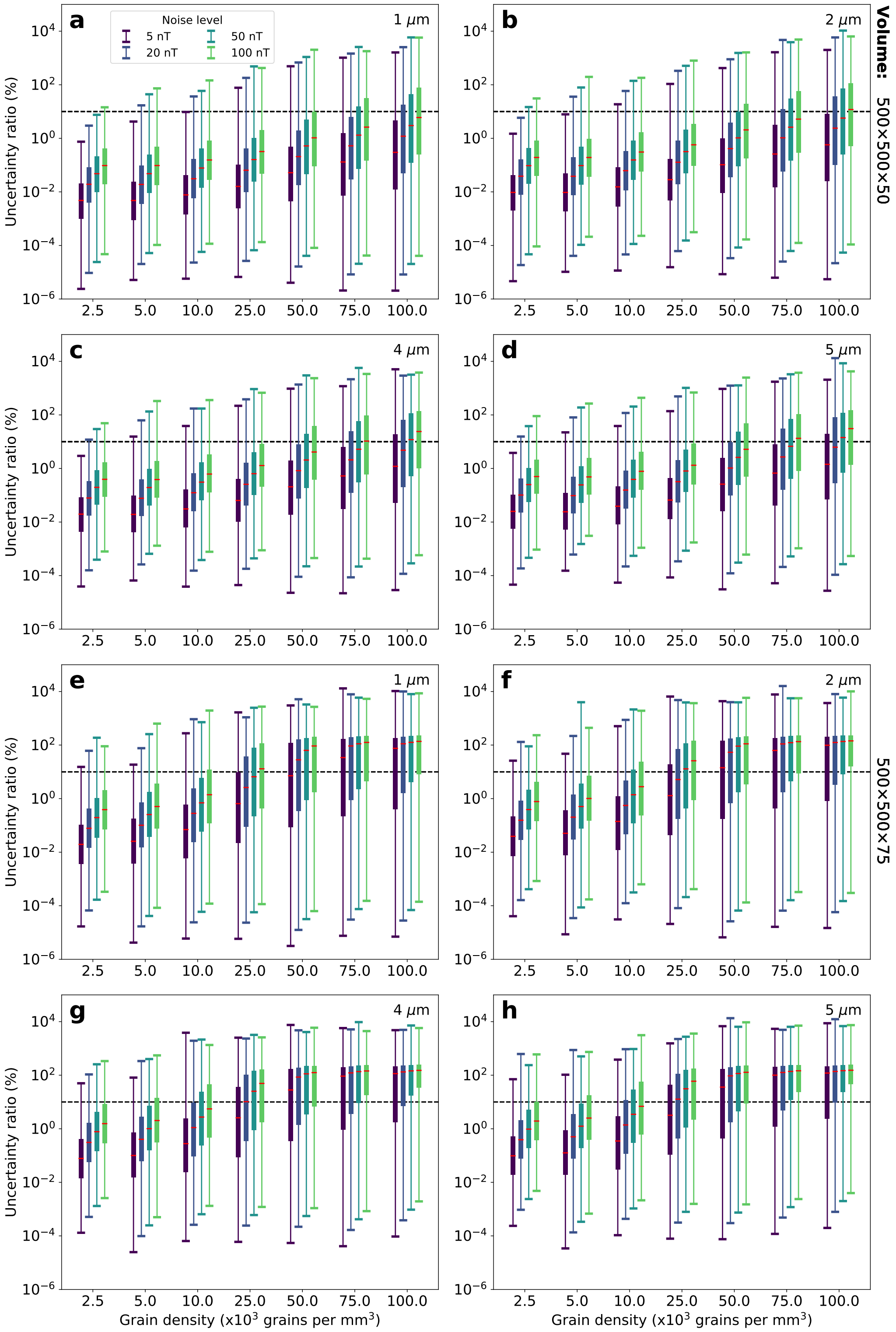


**Figure S1.** Boxplots showing the distribution of the uncertainty ratio in a 500×500 $\mu m^2$ domain. Each panel shows the relation between uncertainty ratio and grain density. The red line in each box-plot indicates the median uncertainty ratio, the bottom and top edges of the solid rectangles show the first and third quartile respectively. The bottom and top of each box-plot shows the minimum and maximum uncertainty ratio respectively per model. The four boxplots per grain density correspond from left to right to four noise levels, *i.e.* 5, 20, 50, and 100 nT. The upper 4 panels (a-d) refer to a 50 $\mu$m thick sample. The lower 4 panels (e-h) refer to a sample with a thickness of 75 $\mu$m. Each set of four panels (a-d or e-h) have a sampling interval of respectively 1, 2, 4, and 5 $\mu$m.

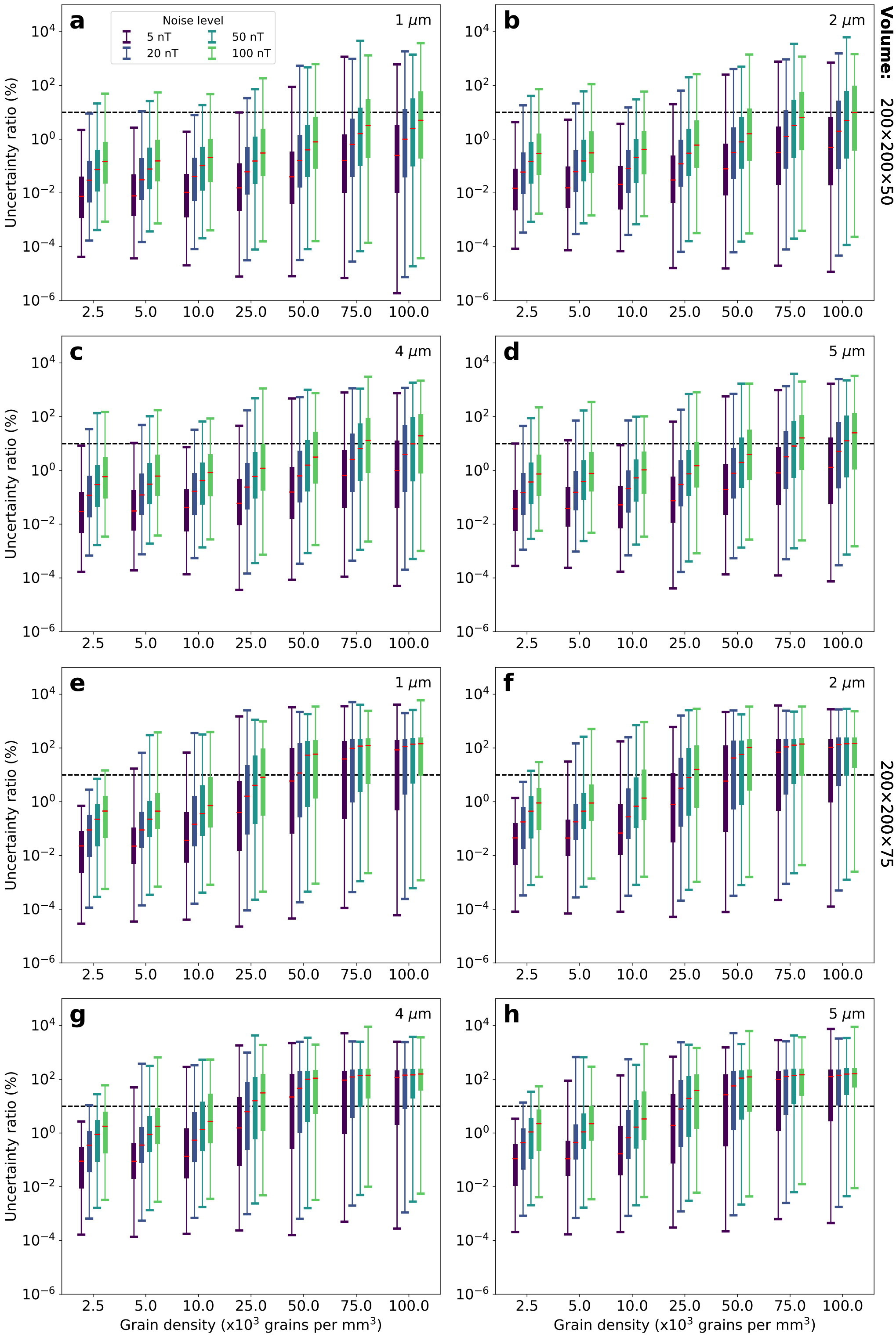


**Figure S2.** Boxplots showing the distribution of the uncertainty ratio in a 200×200 $\mu m^2$ domain, similar to Figure S1.

## 2. Extra signal strength figures

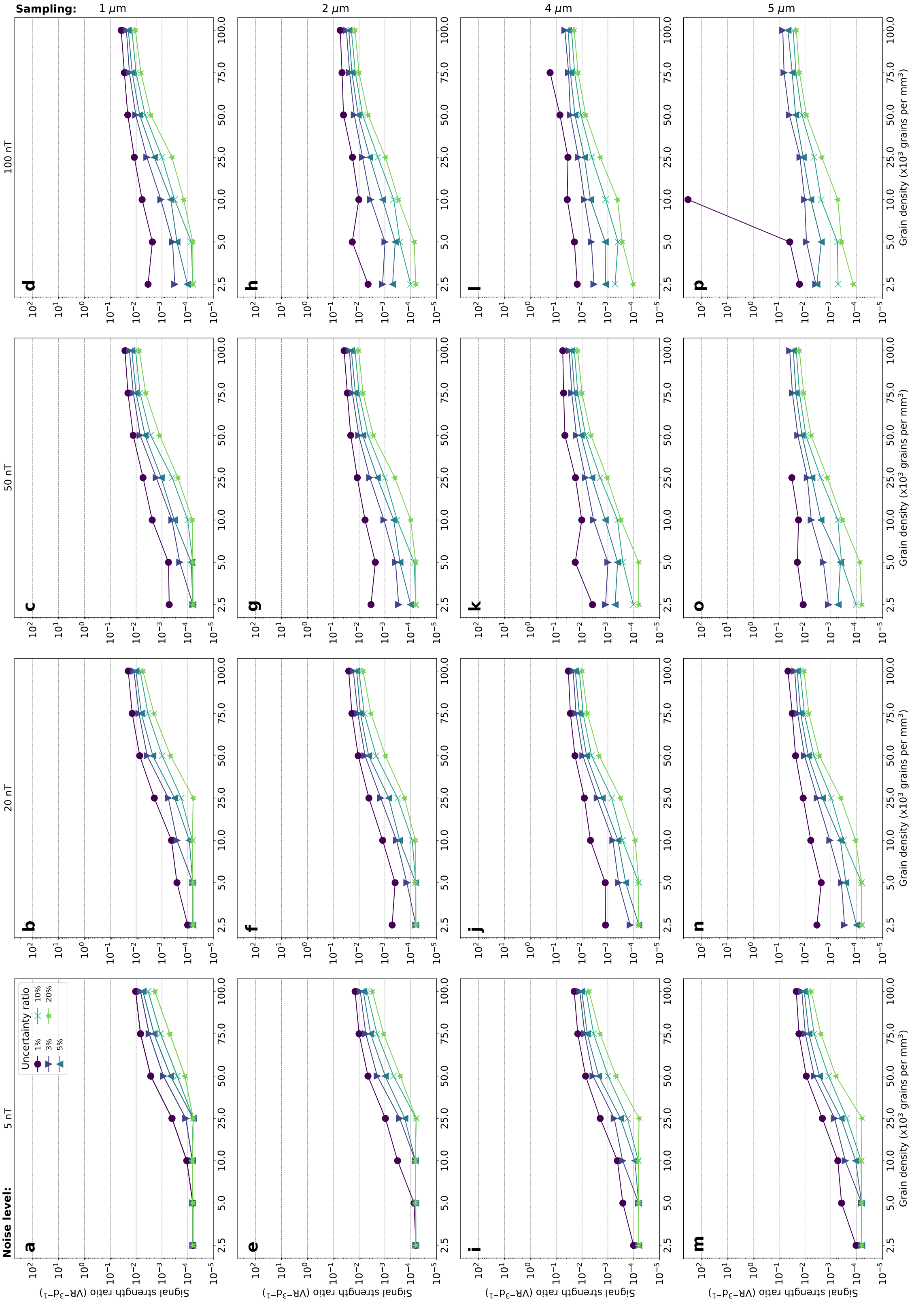


**Figure S3.** 99% resolved SSR plotted against grain density for different uncertainty ratios for the 500×500 $\mu m^2$ sample surface. Each row panels is created with a different sampling interval, that is from top to bottom, 1, 2, 4, and 5 $\mu m$. Each column represents a different noise level, that is from left to right, 5, 20, 50, and 100 nT. Each panel contains five lines corresponding to different uncertainty ratios, namely, 1% (circle), 3% (upper base triangle), 5% (lower base triangle), 10% (cross), and 20% (star). Some points are missing, because no SSR could be found then for which 99% of the grains pass the uncertainty criterion.

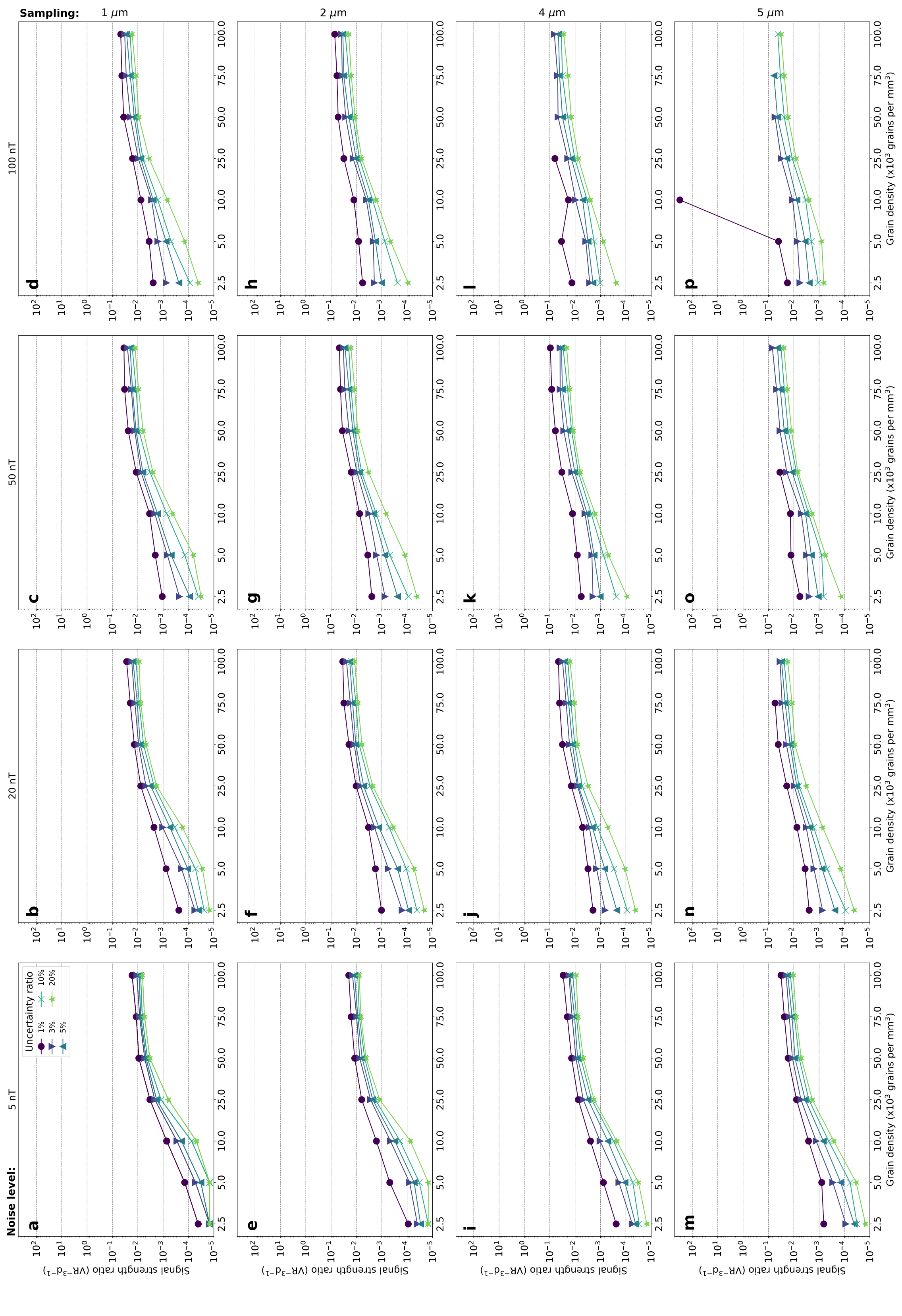


**Figure S4.** See Figure S3, now plotted for a domain of $500 \times 500\ \mu m^2$ and a thickness of $75\ \mu m$.

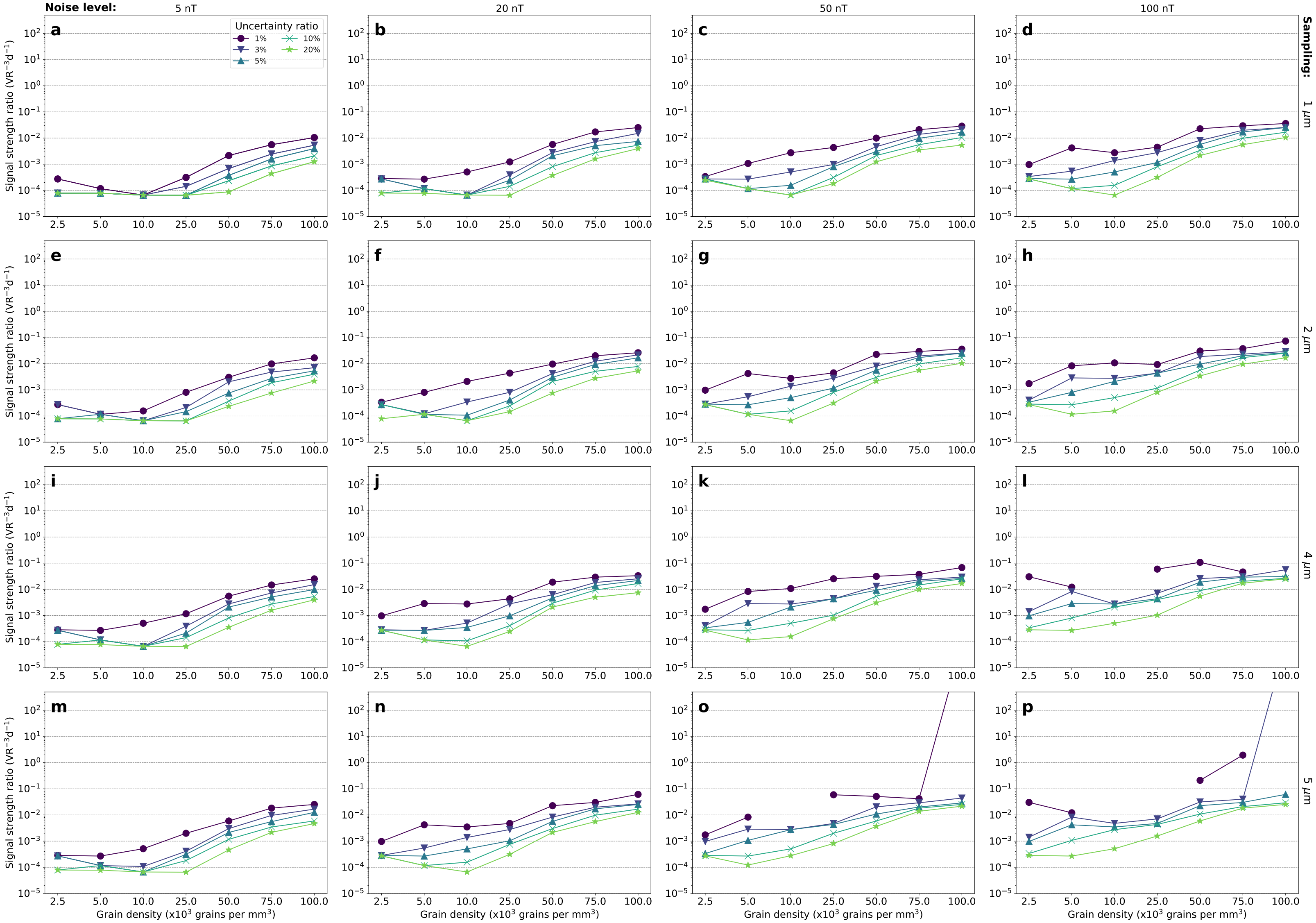


**Figure S5.** See Figure S3, now plotted for a domain of 200×200 $\mu$m$^2$ and a thickness of 50 $\mu$m. The missing point in panel o has a SSR of $3.37\times10^4$ for a grain density of $10^5$ grains per mm$^3$ and an uncertainty ratio of 1%. The missing point in panel p has a SSR of $3.37\times10^4$ for a grain density of $10^5$ grains per mm$^3$ and an uncertainty ratio of 3%.

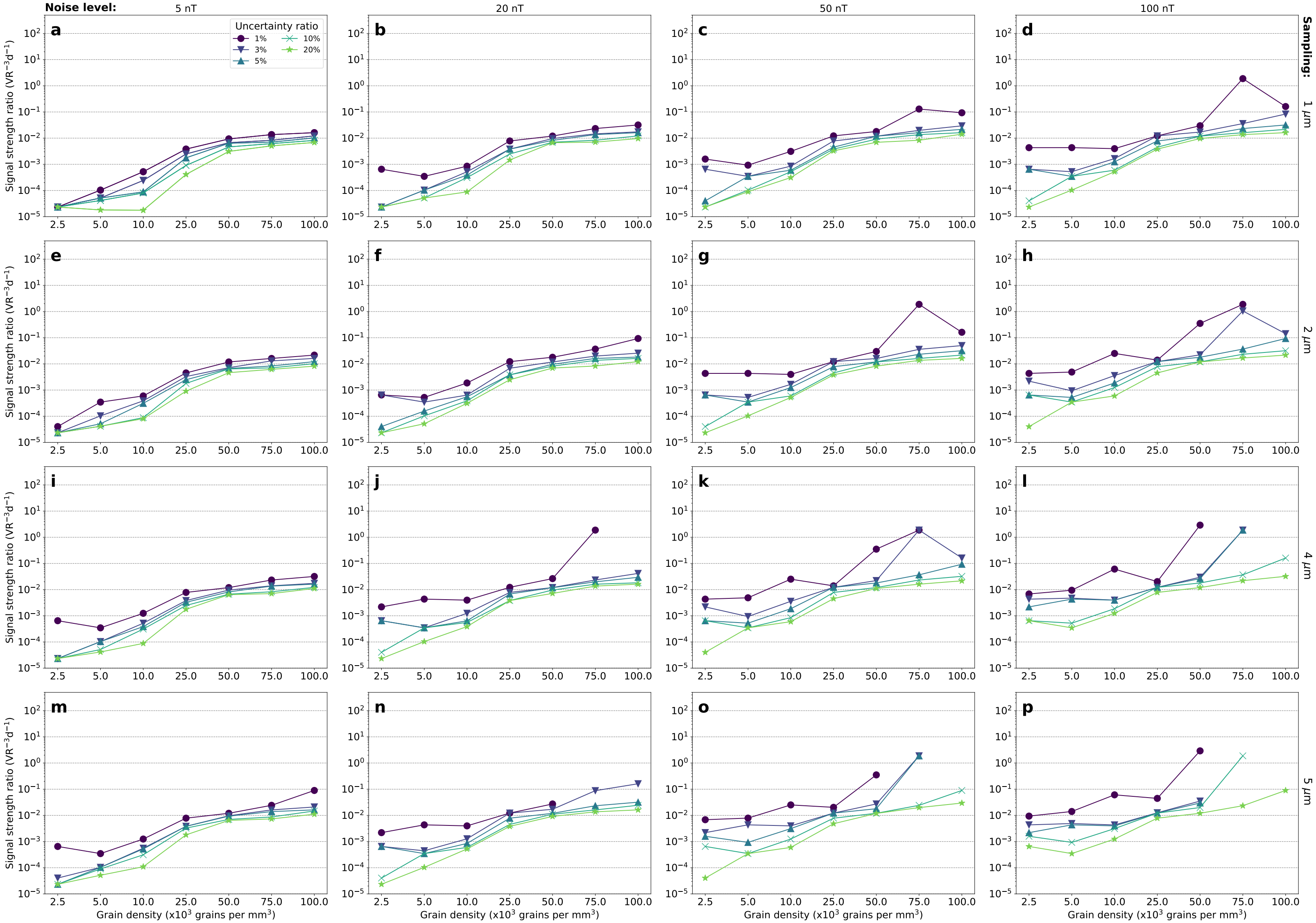


**Figure S6.** See Figure S3, now plotted for a domain of 200×200 $\mu$m$^2$ and a thickness of 75 $\mu$m.